Thermodynamic stability, stoichiometry, and electronic structure of bcc-In_2O_3 surfaces

Peter Agoston* and Karsten Albe
Institut für Materialwissenschaft, Technische Universität Darmstadt, Petersenstr. 32, D-64287 Darmstadt, Germany
(Received 1 January 2011; revised manuscript received 20 March 2011; published 15 July 2011)

The thermodynamic stability of four experimentally observed low-index surfaces of bcc indium oxide (In_2O_3) is investigated by means of density functional theory calculations. The influence of the environment is studied as well as the influence of hydrogen and water. We find that (001) surfaces exhibit the most complex reconstructions. The influence *n*-type dopants (Sn), as well as the in-plane lattice strain is studied for the (001) orientation. Finally, scanning tunneling microscopy images are presented and discussed in light of recent experiments.

DOI: 10.1103/PhysRevB.84.045311 PACS number(s): 68.47.Gh, 31.15.E−, 68.35.Md, 73.20.Hb

I. INTRODUCTION

Transparent conducting oxides (TCOs), such as indium oxide, tin oxide, and zinc oxide, exhibit high electrical conductivities while lacking optical excitations within the visual range. In optoelectronics and especially for optoelectronics applications involving organic materials such as organic light-emitting diodes (OLEDs)[1] and organic photovoltaics (OPVs),[2–4] Sn-doped indium oxide (ITO) is the primary choice.[5–7] For this material free-electron-like conductivities with carrier concentrations of the order of $\sim 10^{21}$ cm^{-3} have been measured.[8]

In addition, In_2O_3 is a suitable material for gas-sensing applications, especially for oxidizing gases such as ozone (O_3), NO_2,[9–12] and Cl_2,[13] but also for reducing gases like CO.[14] The potential of nanostructured In_2O_3 for gas-sensing applications has been demonstrated for a large variety of gas species. ITO is further employed in numerous applications for transparent infrared reflectors,[15] in the field of DNA detection,[16] and as a combustion catalyst for, e.g., methane.[17] Especially in the case of transparent electrical contacts, there is an increasing interest in thin multilayered TCO systems in order to combine different functionalities.

The surfaces of In_2O_3 and ITO have mainly been studied by means of photoelectron spectroscopy techniques (x-ray photoelectron spectroscopy or ultraviolet photoemission spectroscopy)[18–26] and by measuring the gas response (electrical conductivity) against various gas species.[9–14,27] It is found that In_2O_3 surfaces can exhibit variations in the surface composition, but also variations of the dopant concentration (Sn). These changes are often correlated with the measured surface potentials of the materials.[19,20,28,29] In polycrystalline samples the (111) and (001) grain orientations are often observed and the texturing appears to depend on deposition parameters, on the materials, composition as well as the dopant concentration.[5,30–34] It is remarkable that especially in *n*-doped samples the polar (001) surface represents the predominant surface orientation.[5,35]

In the context of the present study, experiments with heteroepitaxial films on yttrium-stabilized zirconia (YSZ) are of special interest, because they address properties of the two predominant orientations, (001) and (111), directly.[23,29,33,34,36–41] Only recently, Morales and co-workers succeeded in obtaining atomically resolved images of the (111) and (001) surfaces of ITO using scanning tunneling microscopy (STM).[34,37] Low-energy electron diffraction (LEED) patterns provide evidence for a (1×1) surface periodicity in both cases. The same authors also found that (111) surfaces remain unreconstructed,[37] whereas (001) surfaces show a rich variety of surface structures, significant disorder, and a dopant-dependent appearance.[34] These results were interpreted on the basis of theoretical studies dealing with the thermodynamic stability.[27,42] According to these studies the (001) surfaces may exist with a cation termination or undergo a dimerization reaction forming a surface peroxide. Several other theoretical studies were mainly concerned with the electronic structure of the ITO surfaces.[43–45]

In contrast to the surfaces of the closely related materials SnO_2[46] and ZnO,[47] the surfaces of In_2O_3 have been studied to a much lesser extent by means of electronic structure calculations. Especially, the stoichiometry variations exhibited by the surfaces as a function of the environment are not well understood. The interaction of water and hydrogen has been studied only for the (001) surfaces, but was not compared with alternative terminations. The effect of tin has not been investigated at all, although there is an apparent influence of the dopants on the surface stability.[19,34]

In this paper, we present results on the relative stability and stoichiometry variations of four experimentally observed surfaces. We study the water adsorption on In_2O_3 surfaces as well as the effect of *n*-type doping on the surface stability. Finally, we discuss the influence of lattice strain on the surface stoichiometry.

II. In_2O_3 SURFACES

Indium oxide crystallizes under standard conditions in the bcc-bixbyite structure, which contains 80 atoms per unit cell. A detailed description of the structure can be found in Refs. 48 and 49. The structure has an alternating anion-cation stacking sequence in {001} directions, where anion and cation layers contain 12 and 8 ions, respectively. Within the cubic In_2O_3 structure there exist two distinct cation positions, which differ by their site symmetry. We shall refer to these different indium sites as In-*b* and In-*d* according to the Wyckoff notation. Note that the site symmetries of In-*b* and In-*d* are S_6 and C_2, respectively.

Surfaces can generally be characterized by their stacking sequence in normal direction according to the established classification scheme for ionic compounds by Tasker.[50,51] Among the low index In_2O_3 surfaces all surface types can be found. The essential features of the stacking sequences

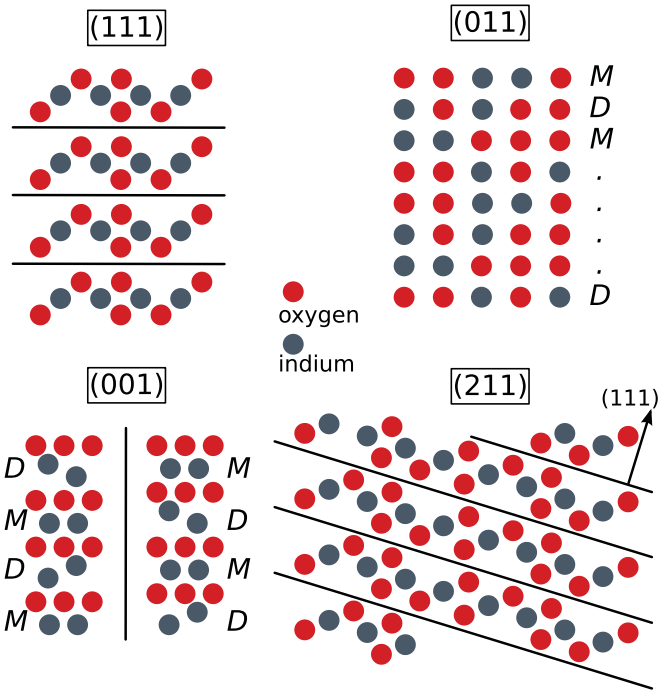

FIG. 1. (Color online) Sketch showing the simplified stacking sequences of low-index In_2O_3 surfaces.

of (001), (011), (111), and (211) surfaces are schematically sketched in Fig. 1. More detailed illustrations can be found in later sections.

In_2O_3 (011) surfaces are classified as Tasker type I with anions and cations in the same layer with stoichiometric composition. Two different terminations exist for the (011) orientation. Due to the existence of two different cation positions, (011) planes with only In-*d* cations and planes containing both In-*d* and In-*b* have to be distinguished. The terminations containing only In-*d* are designated (011-*D*) and those containing mixed sites (011-*M*). The distribution of the anions and cations is slightly different for the two terminations, as indicated in Fig. 1. These two layers are stacked alternatingly and full periodicity is obtained after four repetitions of this bilayer.

In_2O_3 (111) surfaces are of Tasker type II, consisting of stoichiometric trilayers with no net dipole moment. In contrast to the related fluorite lattice, the In_2O_3 (111) surface is rather irregular and its dipole moment vanishes only when averaged over a larger area. There is one type of trilayer within the structure, and full periodicity is achieved after six repetitions.

In_2O_3 (001) surfaces are polar (Tasker type III) and consist of bilayers with a net dipole moment. These types of surfaces have generally a low stability and are unstable in the idealized model of a perfectly ionic compound. Similar to those of (011) surfaces, two different terminations can be distinguished [(001-*D*) and (001-*M*)] based on the content of the different cation sites. The In_2O_3 (001-*D*) cation plane exhibits some buckling, whereas the layer containing mixed sites is perfectly flat (see Fig. 1). The two bilayers are stacked alternatingly and full periodicity is reached after two repetitions of these quadlayers. It should also be noted that the bixbyite structure has inversion symmetry, meaning that the polar (001) surface can be transformed into quasi type II [unlike, e.g., the wurtzite-(0001) surface] by means of appropriate slicing or redistribution of atoms within the surface layers.

Finally, In_2O_3 (211) surfaces have a mixed character, as depicted in Fig. 1. This surface is best described by an array of short (111) facets. The step edges of the so-formed terrasses have a (100) orientation so that consequently the (211) surfaces are partially polar and can be considered as a mix of type II and type III. There is no evident stacking sequence for this orientation. It is, however, possible to slice the structure after each indium layer. This way, three distinct terrace structures can be constructed which make up the basic stacking units. Due to the typical bixbyite distortion these building blocks have slightly different stoichiometries.

III. METHODOLOGY

A. Computational setup

Our results are based on total energy calculations within the plane-wave pseudopotential formalism as implemented in the VASP code.[52,53] We employ the local density approximation (LDA)[54] for the exchange correlation potential and use the projector augmented wave (PAW) method to represent the ionic cores,[55,56] including the In/Sn-4*d* electrons. The cutoff energy is set to 500 eV whereas *k*-point sampling is done with a gamma centered grid with a density of > 20 Å along each periodic reciprocal axis within the surface.

For the slab calculations different supercell geometries were utilized. In the case of the In_2O_3 (001) surfaces the slabs are based on the conventional bcc unit cell. We used slabs containing seven bilayers and 140 atoms in the stoichiometric case. Laterally, the slabs have a size corresponding to (1×1) periodicity and contain either 12 oxygen or 8 indium sites within the surface layer.

In_2O_3 (011) slabs are based on a tetragonal cell with the cubic face diagonal being a new in-plane lattice vector. Again, the slabs have a (1×1) lateral extension and consist of 12 oxygen and 8 oxygen sites within the surface layer. The slab has a thickness of nine stoichiometric layers with a total of 180 atoms for the stoichiometric case.

In_2O_3 (111) slabs were constructed using the standard hexagonal setting. The (1×1) slabs contain six trilayers with stoichiometric composition. Each trilayer consists of 24 oxygen and 16 indium ions resulting in a total number of 240 ions for the stoichiometric case.

Finally, In_2O_3 (211) slabs were created using $[1\bar{1}\bar{1}]$, $[01\bar{1}]$, and [211] as basis vectors, resulting in a supercell containing 480 atoms. Due to computational limitations this cell was resized in the normal direction so that the thickest slab contained only 348 atoms (not stoichiometric).

All slab geometries were constructed in a way to maintain a minimum thickness of 15 Å, resulting in an interaction strength through the slab of less than 0.025 eV per surface atom, which corresponds to ~ 0.003 eV/Å^2 absolute or $\sim 1\%$ relative error in the surface tension. We conducted the respective tests on (001) oriented slabs where the strongest interactions through the slab could be expected. For all calculations, symmetric slabs which did not contain any net dipole moment were employed. The vacuum width was set to > 10 Å, resulting in a

variation of the relative surface tensions below the magnitude of interactions through the slab. The ionic positions were fully relaxed until the forces on each ion were $< 0.01\,\mathrm{eV/\AA}$.

The oxidation state of the surface was checked by means of the Bader analysis.[57] For STM image calculations we used the standard approach by Tersoff and Haman (TH).[58] For these calculations we increased the k-point density in order to obtain a representative Brillouin zone average. Previous STM experiments were obtained by mapping the empty states. Therefore, we integrated the states toward positive energies with respect to the Fermi energy of the system. The image height was adjusted in order to obtain contrast of reasonable detail. The essential features do not depend strongly on this parameter, however.

B. Thermodynamic formalism

Surface tensions were calculated within the grand-canonical potential in the zero-temperature and zero-pressure limits as functions of the oxygen chemical potential according to[59,60]

$$\gamma = \frac{1}{2A}\left\{E_{\mathrm{slab}}^{\mathrm{In}_{2-x}\mathrm{O}_{3-y}} - E_{\mathrm{bulk}}^{\mathrm{In_2O_3}} - x\left(\mu_{\mathrm{In}}^{\mathrm{metal}} + \Delta\mu_{\mathrm{In}}\right) - y\left(\mu_{\mathrm{O}}^{\mathrm{O_2}} + \Delta\mu_{\mathrm{O}}\right)\right\} \quad (1)$$

where μ_i describes the chemical potentials of the respective atomic species i, x and y express the changes of the surface composition, and A is the surface area of the slab. The allowed range of chemical potentials is determined by the heat of formation of the compound via the following equation (at 0 K)

$$\Delta H_f^{\mathrm{In_2O_3}} = \Delta 2\mu_{\mathrm{In}} + 3\Delta\mu_{\mathrm{O}}, \quad (2)$$

where the $\Delta\mu_i$ describe deviations of the chemical potentials from the cohesive energies of the elemental reference phases [$\mu_{\mathrm{In}}^{\mathrm{metal}}$: tbc-In (SG. 136 I4/mmm); and $\mu_{\mathrm{O}}^{\mathrm{O_2}}$: molecular O_2].

Following the ideas described in Ref. 60 we chose the metal-rich regime as the "reliable" limiting case with respect to inaccuracies in the calculation of the compound heat of formation ($H_{\mathrm{In_2O_3}}^{f}[\mathrm{Exp}] = -9.47\,\mathrm{eV}$[61] and $H_{\mathrm{In_2O_3}}^{f}[\mathrm{LDA}] = -10.61\mathrm{eV}$). In the stability diagram we consequently identified the calculated metal-rich extremum with the limiting oxygen chemical potential as calculated with the experimental value.

In the present study, we compare different surfaces of the same material, and expect that the errors due to the exchange-correlation functional mainly act as a fixed (positive) offset on all calculated surface tensions.

For example, the surface tensions obtained by the generalized gradient approximation (GGA) are systematically lower when compared with the LDA data reflecting the overbinding and underbinding of the LDA and GGA, respectively. We recalculated the surface tensions of stoichiometric surfaces with the generalized gradient approximation (GGA) in the parametrization by Perdew, Burke and Ernzerhof (PBE)[62] functional (Sec. IV A) in order to estimate the influence of the exchange-correlation functional.

TABLE I. Surface tensions γ of stoichiometric In_2O_3 surfaces calculated with different exchange correlation functionals and semicore states included or excluded from the valence. The values are given in units of $\mathrm{eV/\AA^2}$.

Surface	LDA	GGA-PBE	GGA-PBE (In-4d)
(111)	0.07(2)	0.05(6)	0.04(9)
(011)	0.09(4)	0.07(7)	0.06(9)
(211)	0.11(8)	0.09(5)	0.08(5)
(001)	0.14(2)	0.11(4)	0.10(2)

IV. RESULTS AND DISCUSSION

A. Stoichiometric surfaces

In the first step we constructed the stoichiometric low-index surfaces (111), (011), (001), (211) and compared their surface energies (Table I). The surface tensions increase in the following order: $\gamma(111) < \gamma(011) < \gamma(211) < \gamma(001)$. It is important to note that this ordering is changed neither by the exchange-correlation functional employed nor by the inclusion or exclusion of the In-4d electrons in the calculations. The order of the surface tensions is in line with the most recent calculations by Walsh and Catlow[45] as well as with the expected behavior for fluorite-derived structures. The corresponding geometries are illustrated in Fig. 2. The polar surfaces have the highest surface tensions [(001), (211)]. While this is expected from a theoretical viewpoint, it is also somewhat contradictory to the very frequent experimental observation of predominantly (001) textured ITO thin films.[5]

In the case of (111) and (011) orientations the surface structures correspond to the simplest possible bulk truncations. Both of these surfaces are built from dipole-free units with bulk stoichiometry. No change of conformation is therefore needed in order to stabilize these surfaces. Consequently, only little surface relaxations are observed. The (111) surface is the overall most stable surface of bcc In_2O_3 followed by the (011) surfaces. The (011-D) termination is by only 1 $\mathrm{meV/\AA^2}$ more stable than (011-M).

In the case of (001), the choice of a stoichiometric surface is more complicated. One obtains surfaces with either half-cation or half-anion terminations. This rearrangement of charges avoids the Coulomb divergence of Tasker type III surfaces. Since In_2O_3 contains 8 In and 12 oxygen sites within one (001) surface unit cell, the resulting stoichiometric terminations contain either 4 cations or 6 anions distributed on 8 cation or 12 anion sites, respectively. Several arrangements of half-filled cation and anion surfaces also involving both (001-D) and (001-M) terminations have been considered and the following is observed:

1. It is more favorable to expose half-filled oxygen layers to the surface, although the difference to the lowest-energy half-indium termination is not very large ($\Delta E \sim 0.02\,\mathrm{eV/\AA^2}$).
2. For both half-oxygen and half-indium, the energy variation for different surface atom arrangements is comparable ($\Delta E \sim 0.025\,\mathrm{eV/\AA^2}$).
3. For half-indium terminations it is energetically more favorable to have a (001-M) as the terminal cation layer($\Delta E \sim 0.016\,\mathrm{eV/\AA^2}$), whereas the opposite is true for half-oxygen terminations ($\Delta E \sim 0.011\,\mathrm{eV/\AA^2}$).

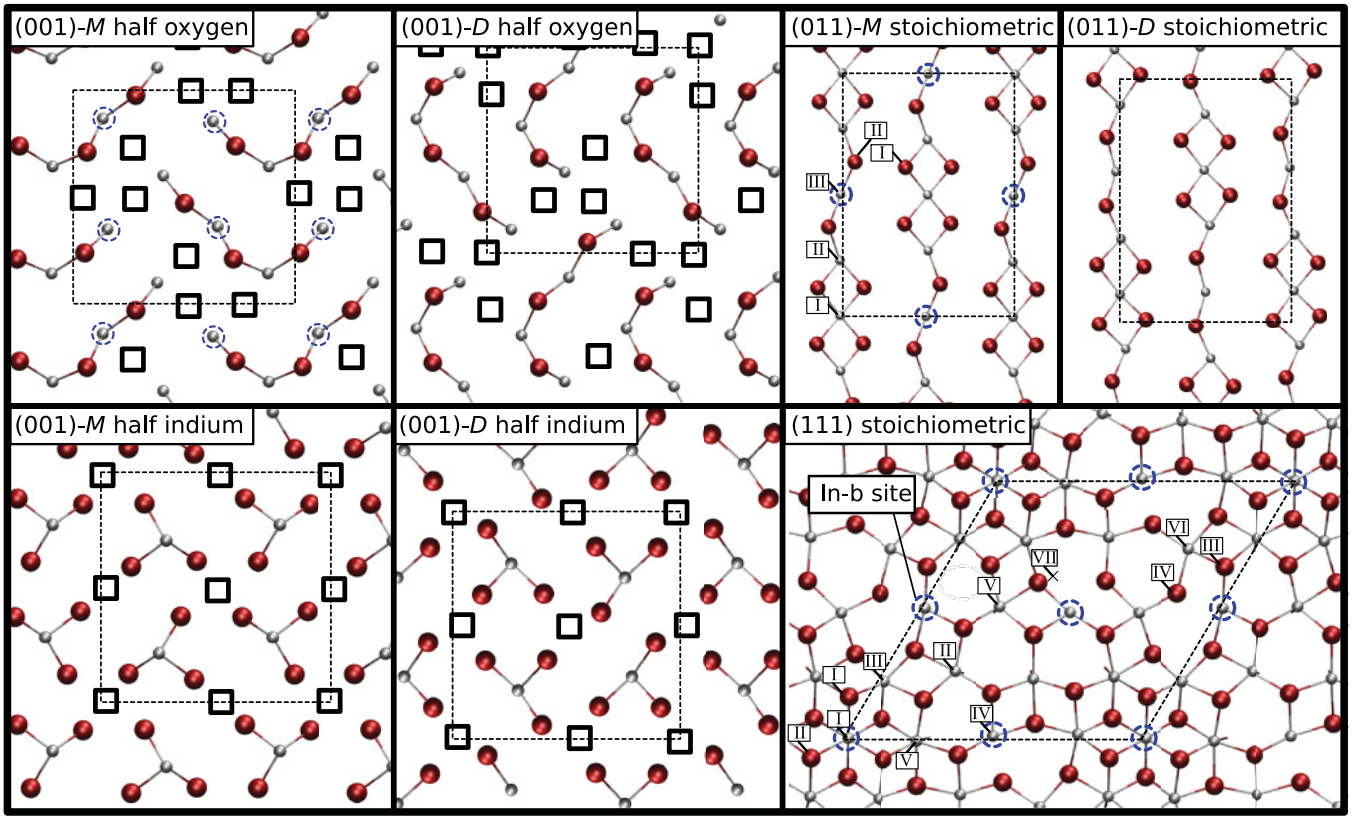

FIG. 2. (Color online) Representation of the stoichiometric (001-M/D), (011-M/D), and (111) surfaces. Large red and small gray balls represent oxygen and indium, respectively. The In-b atoms are circled whereas missing lattice atoms are denoted by black boxes. Numbers indicate specific cation and anion sites. Note that the sites In-I and In-V are sixfold coordinated on (111) whereas the other In are fivefold. On the (011) surface In-I/II are fivefold and In-III is fourfold. (a) (111), (b) (011-M), (c) (011-D), (d) (001-M), (e) (001–D), (f) (211).

We conclude that the stable stoichiometric In_2O_3 (001) surfaces consist mainly of half-filled oxygen planes involving a considerable disorder (because of low energetic differences). Further, the small energetic difference between the most stable half-cation and half-anion terminations implies that areas of both, half-indium and half-oxygen, could coexist. The large density of configurational states in the case of stoichiometric In_2O_3 (001) surfaces implies a significant contribution of entropy. For a more complete modeling of the surface configuration the configurational entropy contributions to the free energy have to be included explicitly by, e.g., the cluster-expansion method. At present we have, however, not attempted such an analysis. It is also clear that the (001) surfaces are unstable with respect to faceting especially into (011) and (111) surfaces.

The (211) surfaces of In_2O_3 are made up of terrace-like structures with mixed (111) and (001) character (see Fig. 5 in Sec. IV B). As it will shown below, stoichiometric surfaces of this orientation are of no particular interest as they are never stable with respect to oxygen-rich or indium-rich surfaces. For completeness, in Table I the value of the most stable stoichiometric variant is listed.

B. Surfaces with stoichiometry variations

Surfaces are generally able to vary their stoichiometry, if the chemical environment changes. Especially in the case of polar surfaces, compositional variations are a means for compensating polarity.

To find the equilibrium compositions of the different surfaces we have calculated for all surfaces a series of slabs with varying numbers of indium and oxygen atoms. From Eq. (2) we obtain surface phase diagrams as functions of the chemical potentials of the constituents. In the case of a two-component system like In_2O_3, the chemical potentials of the constituents are related by Eq. (2), so that only one is an independent quantity. It is convenient to use the oxygen chemical potential, which can be easily converted into the corresponding experimental environmental conditions (p_{O_2}, T) via the ideal gas law and thermochemical tables.[60,63]

The results of these calculations are plotted in Fig. 3. The diagrams show the stability region ranging from $H_f^{In_2O_3}/3$ (oxygen-poor/indium-rich) to zero (oxygen-rich/indium-poor). These limits correspond to the decomposition reaction into the elements $In_2O_3 \rightarrow 2In + 3/2O_2$. The oxygen-rich limit ($\mu_O = 0\,eV$) is usually not achieved in contact with a (di)oxygen atmosphere since most experiments are not conducted at oxygen partial pressures higher than 1 bar but at elevated temperatures. 1 bar of pure oxygen atmosphere corresponds to $\mu_O \sim -0.3\,eV$ at ambient temperature and increases to $\mu_O \sim -0.5\,eV$ at modest heating of 200 °C.

Note that the oxygen-rich side of the diagrams is, however, frequently reached and probably even exceeded when exposed to less-stable oxygen species like atomic oxygen or ozone (O_3).

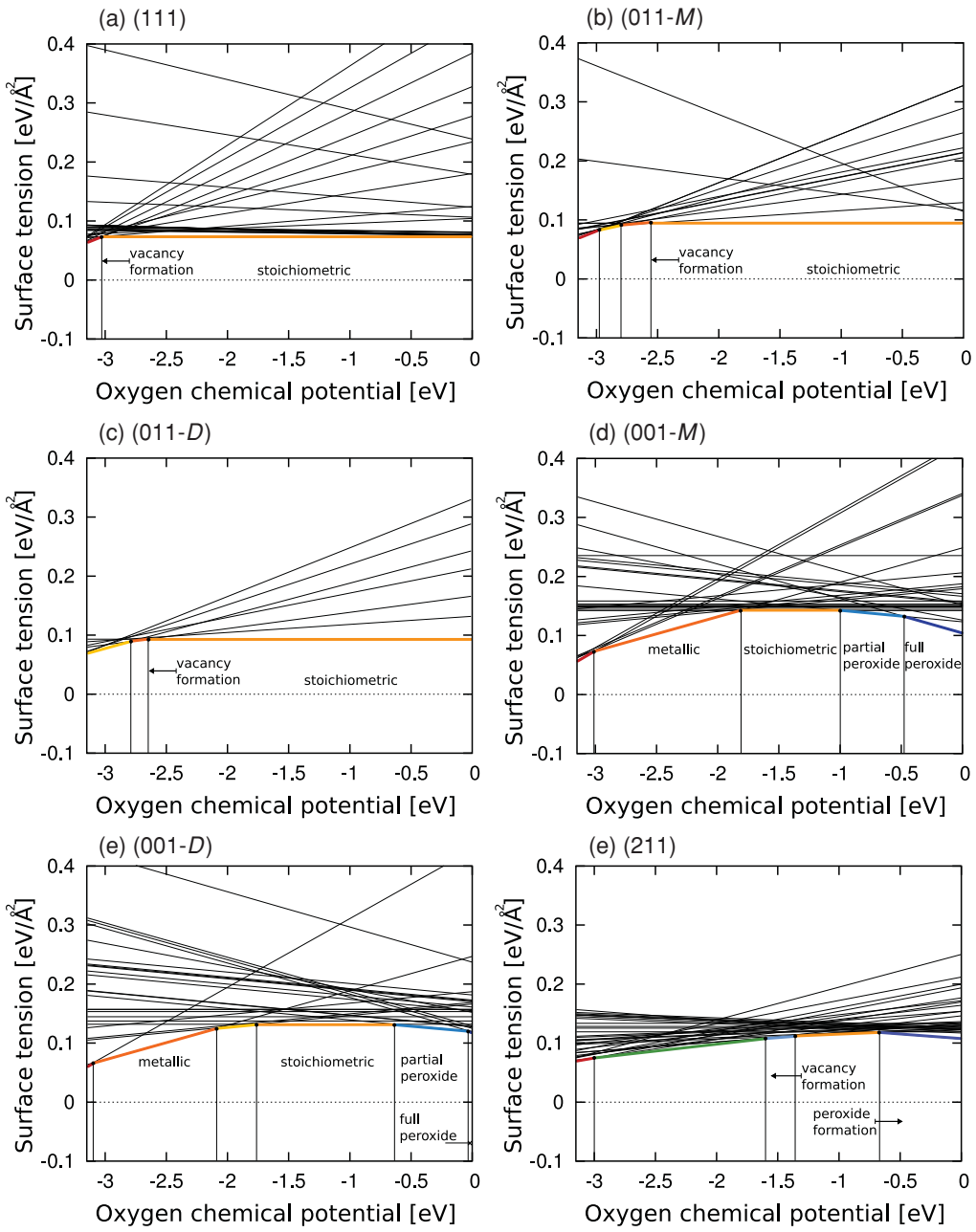

FIG. 3. (Color online) Calculated surface tensions as functions of the oxygen chemical potential for different surfaces of In_2O_3. Black lines denote calculations with various stoichiometries. Colored lines represent the energetically most stable surface reconstruction.

Atomic and even accelerated oxygen can be present in sputtering processes, whereas ozone is frequently used for oxidation of contaminants on electrodes.[64] The lower end of the diagram is reached by simply heating at low oxygen pressure. The reducing limit corresponds to a temperature of 1250 K under UHV (10^{-8} Pa) conditions.

The low-index surfaces of In_2O_3 show stoichiometric variations to rather different extents. Generally, the variability of the stoichiometry depends on the absolute magnitude of surface tension. The higher the surface tension the stronger the propensity toward stoichiometry variations. Larger reconstructions of the surface including stoichiometry variations can be expected when the surface energy per surface atoms is in the range of typical formation energies for point defects.

1. (111) Surfaces

The (111) surfaces exhibit a chemically inert behavior over almost the entire range of oxygen chemical potentials. We calculated slab geometries involving different arrangements of surface vacancies by reducing this surface until all oxygen in the topmost trilayer was removed. In addition, vacancy geometries involving the topmost but also the second oxygen layer were considered. The surface composition of the (111) surface remains intact up to a chemical potential of $\mu_O \sim -3.0$ eV [Fig. 3(a)].

The surface with a small stability range at low oxygen chemical potential corresponds to the situation with all oxygen removed from the surface located in the upper part of the

(111) terminal trilayer. This strongly reduced (111) surface exhibits mainly threefold and onefold coordinated indium at the surface. It is important to note that also several other reduced (111) surfaces become stable with respect to the stoichiometric surface at a very similar oxygen chemical potential (denoted by thin black lines). More generally, this point marks the oxygen chemical potential at which the surface oxygen vacancy formation energy vanishes. This behavior suggests a continuous reduction of the surface on an atomic level by the increasing concentration of surface oxygen vacancies up to a full depletion. This behavior is very similar to that found in CeO_2,[65] a structurally related material.

The oxygen surface vacancy concentration steadily increases with decreasing oxygen chemical potential up to the point where the phase transition is indicated in Fig. 3(a). At this point the surface has reached its fully depleted state. This behavior indicates that the surface reduction is not related to a phase transition associated with a nucleation process.

Note that the vacancy formation energy considerably varies for different oxygen positions within the surface unit cell and is lowest for the oxygen denoted O-I in Fig. 2. As a consequence oxygen can be removed from these positions at considerably lower oxygen chemical potentials and furthermore it implies a locally inhomogeneous vacancy distribution on the surface.

On the oxygen-rich side, it is energetically not favorable to add surplus oxygen at any site. We considered the attachment of atomic oxygen and dimeric oxygen at various locations on the surface and always observed a positive excess energy even under oxygen-rich conditions.

2. (011) Surfaces

Chemically, (011) surfaces show stoichiometry variations very similar to those of (111) surfaces. Only under harsh reducing conditions) do these surfaces exhibit an oxygen depletion on the surface by the occurrence of surface oxygen vacancies. The difference in comparison with (111) is that the reduction point is located at a slightly higher oxygen chemical potential ($\mu_O \sim -2.6\,\text{eV}$). As for (111), also in the case of (011) surfaces the transformation between the depicted phases [Fig 3(b) and 3(c)] is rather continuous. The different line segments correspond to no unique reconstruction below the reduction point and infinitely many can be constructed in between those. Nevertheless, also on the (011) surface, oxygen positions are associated with different vacancy formation energies depending on their coordinations.

The oxygen species on the stoichiometric (011) surfaces are all threefold in geometric arrangements which vary from close to trigonal planar to trigonal pyramidal. Oxygen vacancies are preferentially produced in the latter geometry (e.g., O-I in Fig. 2). Because this oxygen geometry predominates in the case of (011) surfaces, oxygen vacancy formation is easier in comparison with the (111) surface where a major fraction of surface oxygen is fourfold coordinated. The reduction is also slightly different when (011-*M*) and (011-*D*) are compared. This is due to the different oxygen geometries in the two terminations. For example, on the (011-*M*) surface it is favorable to remove all oxygen atoms, which are depicted in Fig. 2 (12 oxygen per surface unit cell) in the metal-rich limit. This surface consists of only the remaining one-fold and twofold coordinated In chains along the $(1\bar{1}0)$ direction and is represented by the lowest line segment in Fig. 3(b) ($\mu_O < -3\,\text{eV}$). In comparison, the lowest line segment in the case of the (011-*D*) termination has still a 4/12 oxygen per surface unit cell remaining and full oxygen depletion is not favorable under any condition.

As in the case of (111), on the oxygen-rich side we could not identify any stable structures by the attachment of atomic or molecular oxygen.

3. (001) Surfaces

The In_2O_3 (001) surfaces exhibit the most significant variations of stoichiometry due to their comparatively large surface tension. We have adopted the ideas of Golovanov *et al.*[27] and Zhou *et al.*[42] and compared their results with several alternative structures in order to obtain the phase diagrams which are shown in Figs. 3(d) and 3(e).

Under reducing conditions it is most favorable to simply remove all surface oxygen, leaving behind a complete metal cation termination. This composition has a stability range of ~1eV in the diagrams of both variants, (001-*M*) and (001-*D*).

The cation arrangement of the two terminations is illustrated in the top part of Fig. 4. While the indium atoms in the (001-*M*) terminal layer are all threefold coordinated, in the case of (001-*D*) it is a composition of twofold, threefold, and fourfold coordinated In. This variation of coordination also leads to a variation of the position of In atoms normal to the surface. The energetic difference between the two terminations is negligibly small in the reduced state.

At the lowest oxygen chemical potentials, additional small line segments can be found which correspond to even stronger reduced cation terminated surfaces with additional surface indium on top (not illustrated). This can be thought of as a nucleation of metallic tetragonal-body-centered In and becomes favorable even before the stability limit is reached.

At high oxygen chemical potentials oxygen-rich surfaces occur, a feature which is not found for (111) and (011) surfaces. This is particularly interesting considering that In_2O_3, but also other typical *n*-type TCOs like ZnO, SnO_2, or Ga_2O_3 are predominantly oxygen deficient and no superoxides or peroxides of indium are known.

The stabilization of the oxygen-rich surface terminations occurs by dimerization of oxygen in the topmost plane as was already suggested by Golovanov *et al.*[27] This surface can be understood by the formation of a local peroxide. If we assume the oxidation state O^{1-} in the peroxo-anion configuration, the surface charge is formally reduced to half of a bulk oxygen layer which is favorable in order to avoid the Coulomb divergence of polar surfaces.

The lower part of Fig. 4 shows the fully dimerized surfaces placed on the two types of indium planes. Interestingly, the fully dimerized (six dimers per unit cell) surface is stable on only the (001-*M*) termination, for geometric reasons.

In the case of the (001-*M*) surface with peroxides, all cations below the dimers attain a sixfold coordination as it is found in the bulk. In contrast, it is not possible to arrange the dimers in a way so that the bulk coordinations are obtained in the case of (001-*D*). This geometrical constraint leads to a

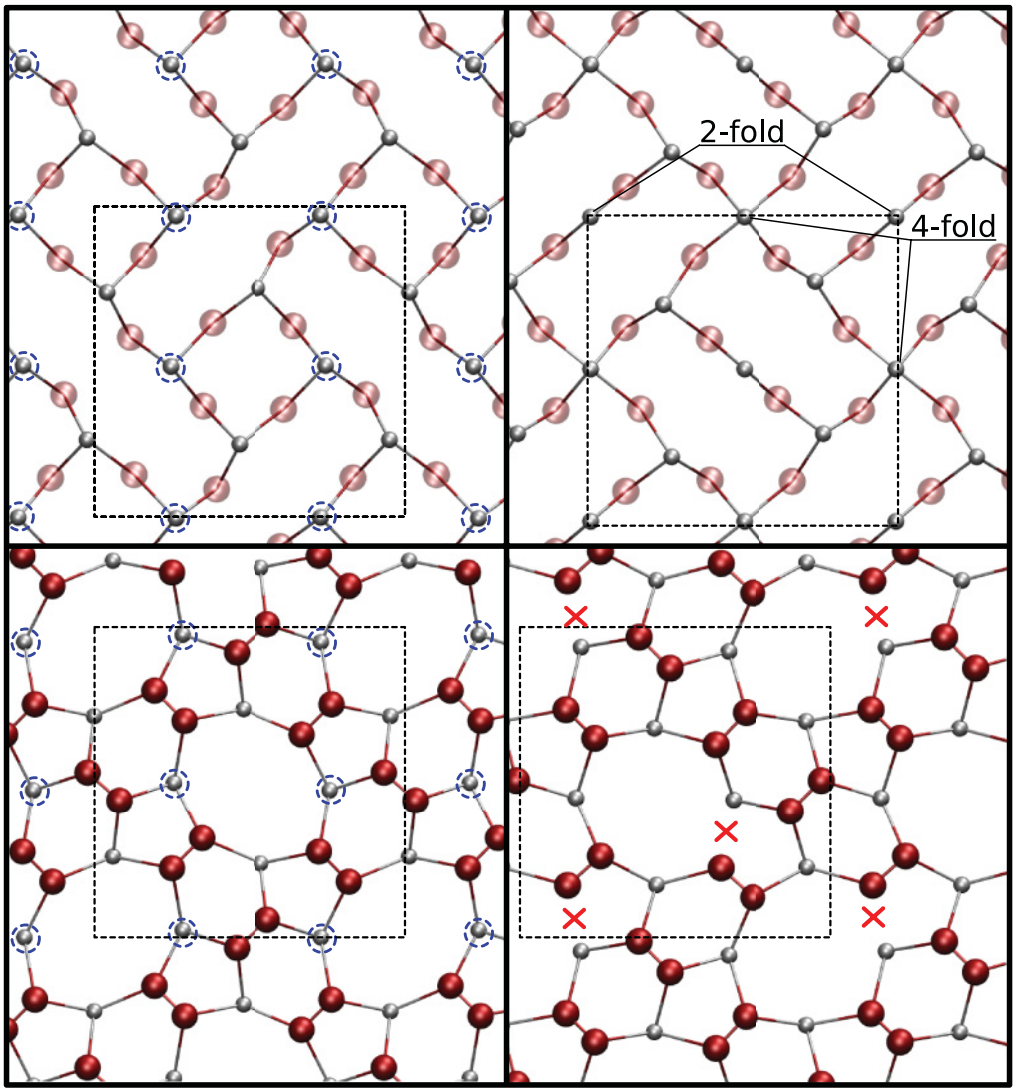

FIG. 4. (Color online) Representation of the metallic oxygen-depleted (top) and most oxygen-rich peroxide reconstructions for (001-*M*) (left) and (001-*D*) (right), respectively. Large red and small gray balls represent oxygen and indium, respectively. A red cross indicates the location of an elongated bond showing the incommensurability of the full peroxide termination with the (001-*D*) cation sublayer.

strained peroxide surface layer (see Fig. 4, bottom right) and a higher surface tension.

More generally, the (001-*D*) termination shows a tendency toward oxygen poorer surfaces. This is also manifested in the occurrence of another oxygen-deficient phase between the metallic and stoichiometric which is not present in the case of (001-*M*). The stabilizing feature is the highly undercoordinated (twofold) In on (001-*D*), which binds oxygen anions more tightly and leads to the possibility of a partial reduction (1/3 oxygen coverage).

Between the full peroxide and stoichiometric surfaces another intermediate partially dimerized surface exists for both (001-*M*) and (001-*D*). These surfaces consist of four oxide anions and two dimers per surface unit cell. The total negative charge of these surfaces equals that of stoichiometric and full peroxide surfaces and is therefore stable according to the Tasker classification. It is, however, noteworthy that not all possible charge compensated surfaces have a stability range.

For example, another charge-compensated and partially peroxide-covered surface can be constructed with four dimers and two oxide anions, which, however, exhibits a considerably larger surface tension and therefore no stability range.

4. (211) Surfaces

There are three different terminations in the case of In_2O_3 (211) surfaces. Their structure as well as their stoichiometry variations are, however, very similar. Figure 5 shows the general structure of these surfaces in a side view. The crystallographic directions are denoted in the figure in order to indicate the relationships to the (001) and (111) faces.

The structure of this surface is a series of facets, with the long edges being (111) and the step edges being the extensions of oxygen (001) planes. The step edges themselves have $[\bar{1}10]$ alignment in the figure. These edges are characterized by a row of protruding oxygen atoms which are circled in the figure. The three different terminations differ mainly by the number

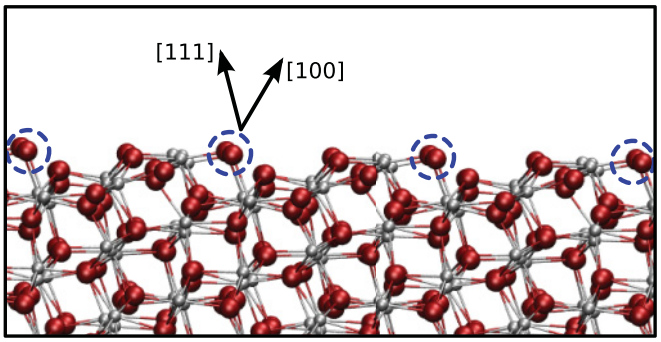

FIG. 5. (Color online) Representation of one stoichiometric In_2O_3 (211) truncation. Large red large and small gray balls represent oxygen and indium, respectively. The circled oxygen rows are those which can be removed (reduction) or form peroxo-anions (oxidation), depending on the given oxygen chemical potential.

of oxygen atoms within these edge positions, and only one cut is presented in the figure.

The stoichiometry variations of these surfaces can be understood as a combination of the observations made for (111) and (001) surfaces. While on the (111) faces no variation is energetically favorable (except for vacancy formation at low μ_{O_2}), the edges which have (001) character can be reduced and oxidized similarly to the (001) surfaces. Oxygen can be removed, resulting in reduced edges, whereas it is favorable to accommodate extra oxygen in the form of a peroxide at the edges. Since the edges only make up a smaller fraction of the total surface area the stoichiometry variations are weaker when compared with (001). Due to the presence of large areas with (111) character the lower surface tension in comparison with (001) surfaces can be explained. Finally, we note that the chemistry of (211) surfaces also closely resembles that of (111) step edges due to the structural similarities.

V. WATER

A. Water adsorption on stoichiometric (111) and (011) surfaces

The (111) and (011) surfaces are chemically almost inert with respect to oxygen, but it remains to be shown to what extent these surfaces can adsorb water and promote dissociation of the molecules.

On the stoichiometric (111) and (011) surfaces, species with various coordinations can be encountered. In the case of (111) surfaces, anions are either fourfold or threefold coordinated while cations have sixfold or fivefold coordination (see Fig. 2). In the case of (011-M/D), all anions are threefold coordinated in the topmost layer whereas fivefold and fourfold indium can be found.

In Table II the adsorption energies of water on various sites of these two surfaces are listed. The site numbers in this table correspond to those depicted in Fig. 2. They label the cations and anions on which the oxygen and hydrogen atoms of the water molecule attach to the surface.

Depending on the respective site, the adsorption energies can vary, but are on average of the same magnitude for both surfaces. The adsorption energies are in the range of $H_f^{H_2O}/2$ which makes the dissociation possible. In the case of (111) surfaces, water dissociation is mainly possible where fivefold indium and threefold oxygen are found in close proximity. Since such sites are present on only a small fraction of the total surface area, (111) surfaces exhibit a spatial separation of regions with different chemical activity.

TABLE II. List of adsorption energies (in eV) for water on stoichiometric (111) and (011) surfaces. The indium and oxygen atoms to which the oxygen and hydrogen atoms of the water molecule attach on the surface are given. The sites are marked in Fig. 2. The labels d. and n.d. indicate whether it is a dissociated or nondissociated geometry of the water molecule.

(111)		(011 − M)	
$E_{ads}^{H_2O}$(eV)	Position	$E_{ads}^{H_2O}$(eV)	Position
−0.74	In_{III}/O_{II} (d.)	−1.02	In_{I} (n.d.)
−1.42	In_{III}/O_{I} (d.)	−0.97	In_{II} (n.d.)
−1.13	In_{VI}/O_{III} (d.)	−1.03	In_{III} (n.d.)
−1.18	In_{III} (n.d.)	−0.81	$O_{I/II}$ (n.d.)
−0.95	In_{VI} (n.d.)	−1.26	In_{III}/O_{III} (d.)
−0.70	In_{VI} (n.d.)	–	–
−0.41	O_{I} (n.d.)	–	–
−0.71	O_{IV} (n.d.)	–	–
−1.00	In_{IV} (n.d.)	–	–

In the case of (011) surfaces, a similar behavior can be observed. In this case, the dissociation can occur only on fourfold coordinated In. The separation of sites where dissociation is observed is not so large when compared with that of the (111) surface. The surface unit cell of stoichiometric (011) is a centered tetragonal cell of less than half the size of the hexagonal (111) unit cell.

Further, it is found that the separation of the two hydroxyls which are created upon water dissociation tend to stay bound. For example, the energy excess due to the separation of two vincinal hydroxyls on (111) surfaces is +0.68 eV.

From the adsorption energies the desorption conditions for water can be inferred for the two surfaces. We estimate the desorption temperatures as functions of the water gas partial pressure by the condition[60,63]

$$\Delta G_{ads}^{H_2O}(T, p_{H_2O}) = 0, \tag{3}$$

i.e., the conditions at which the free energy of adsorption vanishes. Considering the most strongly binding sites they are $T = 700$ K and $T = 350$ K at 1 atm and UHV, respectively for (111). In the case of (011) surfaces these values are somewhat smaller, with $T = 640$ K and $T = 290$ K, respectively.

B. Hydrogenated (001) termination

Since the nonreconstructed (001) surface has a high energy, reconstructions and variations of surface composition were necessary for its stabilization. If now water or hydrogen is brought into contact with this surface, these species can react and stabilize the surface and compete with those alternative mechanisms, like the peroxide formation. For the (001) surface and similarly for the (211) orientation it is therefore important to clarify the conditions under which the different compensation mechanisms are operational.

We calculated the surface tensions of the fully hydrogenated and oxygen-rich In_2O_3 (001) surfaces as functions of the

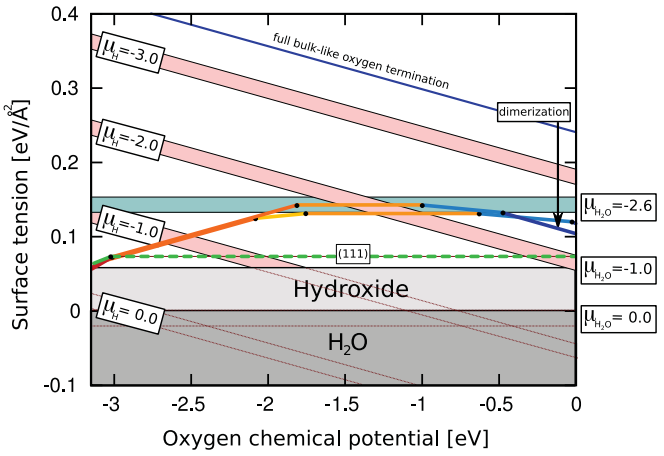

FIG. 6. (Color online) Phase diagram of the (001) surfaces including the fully hydrogenated surfaces represented by bars at different isovalues of hydrogen and water chemical potentials. The width of the bars corresponds to the surface tension difference between (001-M) and (001-D). The chemical potentials are given with respect to the total energy of the isolated respective molecules. The thermodynamically limiting surface tension is given at the oxide/hydroxide boundary ($\mu_{H_2O} = -1.01$ eV), which is indicated by the shaded area.

chemical potentials of hydrogen and water. These surfaces are obtained by dissociatively adding one monolayer of water to the stoichiometric surface or dissociating a hydrogen molecule on each dimer of the oxygen-rich (peroxide) surfaces. The resulting surface contains 12 hydroxyls per surface unit cell. The surface tensions are plotted in Fig. 6 for different hydrogen chemical potentials (diagonal isolines). The widths of the bars shown correspond to the difference in surface tension between the hydrogenated (001-M) (top edge) and (001-D) (lower edge). Overlaid in the same figure are the phase diagrams of (001-M) and (001-D) as well as the (111) surfaces for the hydrogen-free case.

Evidently, the adsorption energy with respect to the isolated hydrogen molecule and the oxygen-rich surfaces is very high, as can be seen from the difference of the last line segment of the In_2O_3 (001) phase diagrams (full peroxide termination) and the isoline at $\mu_H = 0.0$ eV. The adsorption energy amounts to $\sim$4.5 eV per hydrogen molecule. The considerably larger adsorption energy of hydrogen compared with the formation enthalpy of a water molecule warrants the dissociative adsorption process ($H^f_{H_2O,g}$[Exp] = 2.50 eV and $H^f_{H_2O}$[LDA] = 3.12 eV). Starting with a stoichiometric surface and adsorbing water molecules instead, still a large amount of energy ($\sim$2.5 eV per water molecule) is gained. This value should be compared with those for nonpolar surfaces (Table II).

In fact, the occurrence of a negative surface tension in a wide range of the oxygen and hydrogen chemical potentials indicates the destabilization of the material toward the formation of competing phases, namely water and the hydroxide [$In(OH)_3$]. Consequently, the phase boundaries toward these competing phases have to be considered as extrema for the chemical potentials of water or hydrogen in order to obtain the maximum stability of the (001) surfaces but at the same time maintain the thermodynamic stability of the bcc In_2O_3.

As competing phases we have considered gaseous water and indium hydroxide in ReO_3 modification.[66,67] The heat of formation was obtained within the LDA to be consistent with the surface phase diagram. The corresponding thermodynamic constraints are

$$\Delta 2\mu_H + \Delta\mu_O \leqslant \Delta H_f^{H_2O}, \tag{4}$$

$$\Delta\mu_{In} + 3\Delta\mu_O + 3\Delta\mu_H \leqslant \Delta H_f^{In(OH)_3}. \tag{5}$$

The boundary lines of the phase transitions are given in terms of a water chemical potential, which is counted with respect to the energy of a cold and isolated water molecule. The phase transition toward the hydroxide is calculated at $\Delta\mu_{H_2O} \sim -1$ eV and given by the reaction enthalpy of the water addition reaction,

$$2In_2O_3 + 3H_2O \rightleftharpoons 2In(OH)_3, \quad \Delta H_f = -3.1\,\text{eV}, \tag{6}$$

assuming that the temperature dependencies of the free energy of the solids are weak or cancel each other. Note that the boundary is not along a constant hydrogen potential but along a constant water potential, shown in Fig. 6 as the boundary to the shaded area. For chemical potentials of water/hydrogen lower than this boundary it is more favorable for the material to convert into hydroxide.

The stability of the hydrogenated surface termination can now be compared with the (intrinsic) terminations described in Sec. IV B along the hydroxide/oxide boundary line. Notably, the hydrogenated surface is the most stable compared with all other phases of (001) and energetically very close and even lower than the (111) surface, also shown in Fig. 6. Note that the estimated correction to the In_2O_3 (111) surface tension due to hydroxylation is small ($\sim$ 0.01 eV/Å) and therefore considered in the figure.

To fully remove water from the surface in equilibrium, its chemical potential has to be set to $\mu_{H_2O} \geqslant -2.6$ eV. This water potential corresponds to a temperature of $T \sim 1200$ K at 1 atm and $\sim$580 K under UHV. The high equilibrium desorption temperatures of water indicate the facile and persistent hydroxylation of (001) surfaces, which is very distinct from the behavior of the nonpolar surfaces.

We stress that the desorption of water, but also the hydroxide formation, could be prevented by the presence of kinetic barriers so that all values are to be understood as equilibrium estimates. Ideal growth conditions of films with a (001) orientation are given at a water chemical potential at or little beyond the phase boundary toward the hydroxide ($\mu_{H_2O} \sim -1$ eV).

Finally, we remark that besides the hydroxylated surface we have also tested slabs with hydride terminations (negatively charged hydrogen on top of a cation layer). Surfaces of this kind are plausible from a electrostatic point of view; hydride ion incorporation in the form of point defects has already been proposed for In_2O_3. We find, however, that this type of surface termination is unstable even at hydrogen rich conditions and oxygen-poor conditions.

TABLE III. Surface stresses for four different (001) surfaces calculated with two different XC functionals at the calculated equilibrium lattice constant. The values are given in units of meV/Å^2.

Phase	LDA	GGA-PBE
Metallic	−93.80	−64.04
Stoichiometric	−14.56	−2.71
Peroxide	−501.45	−416.18
Hydroxylated	+22.41	+10.20

VI. SURFACE STRESS

In the past, a significant number of studies have dealt with epitaxial In_2O_3 films.[23,29,33,34,36–41] Especially, the morphology of (001) surfaces is rather diverse and depends on the respective growth conditions, doping level, and film thickness. For example Bierwagen and Speck[41] have reported that the most homogeneous films can be obtained at rather reducing conditions whereas n-type doping generally improves the homogeneity. As a substrate material YSZ is most frequently used, which introduces a tensile stress in the In_2O_3 films.[33] When cracking occurs due to the in-plane stress, cleavage propagates along ⟨011⟩ directions which is plausible because (111) surfaces have the lowest surface energy.

In this section, we further explore the influence of in-plain strain $\epsilon_{\text{in-plane}}$ on the surface stability and composition for the case of (001) surfaces. The reason for these studies is the observation of a relatively large surface stress within calculations of oxygen-rich (001) (peroxide) surfaces. This finding is in line with the noncommensurability of the peroxide termination noted already in Sec. IV B. The dimers exert a compressive stress at the surface in order to maximize their attractive electrostatic interaction to the layer below. For the same reason the dimers of the peroxide termination show a pronounced inward relaxation, lowering their position normal to the surface in comparison with the oxide anions. By virtue of this observation the surface in-plane strain is expected to have a more pronounced effect on the peroxide surfaces when compared with other surface phases of this orientation. The calculated surface stresses for different phases of the (001-M) termination are listed in Table III at the calculated equilibrium lattice constant. The surface stresses follow a similar trend for LDA and GGA-PBE, despite the differing lattice constants obtained by the two approximations.

The surface stress σ_i^s is determined by two factors according to Shuttleworth[68] and can be written as

$$\sigma_s = \gamma_i^s + A\frac{\partial \gamma_i^s}{\partial A} = \gamma_i^s + \frac{\partial \gamma_i^s}{\partial \epsilon_{\text{in-plane}}}. \quad (7)$$

The first part is the contribution due to the surface tension γ_s while the second part describes the change of surface tension with strain. As we are interested in only the changes of the phase transitions between different phases the surface tension drops out of Eq. (7) because of the condition $\gamma_i = \gamma_j$ at the point of the phase transition between phases i and j. Variations of the phase transition as a function of the chemical potentials can therefore occur only due to a different strain derivative of the surface tension for two phases. This quantity corresponds to the difference in the surface stresses for two phases.

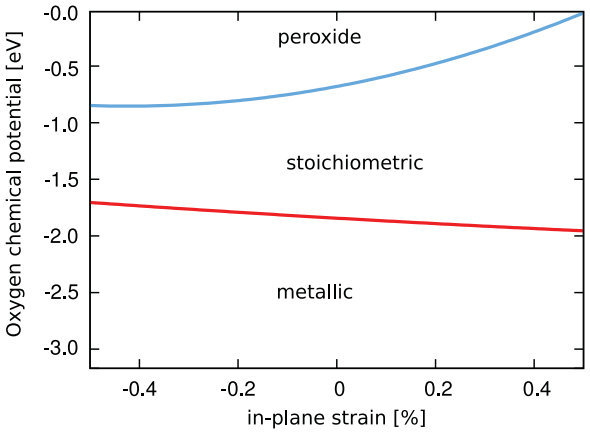

FIG. 7. (Color online) The strain-dependent surface phase diagram for the In_2O_3 (001-M) surface including only the predominant phases.

Thus, the surface phase diagrams presented in Sec. IV B are generally a function of the in-plane strain (the normal direction is always assumed to be stress free) with the surface stress being the corresponding conjugated thermodynamic variable. In the case of a non-varying surface stress for different phases only a constant offset must be added to the surface tensions.

To illustrate the strain-dependent behavior more clearly, we recalculated the phase diagram for the (001-M) surface, considering only the most stable metallic, stoichiometric and full peroxide surfaces. A strain was applied on the surface plane with full ionic relaxation. The phase diagrams were then recalculated using Eq. (2), and the thus obtained phase boundaries as a function of strain are plotted in Fig. 7.

According to the differences in surface stresses the stability of the dimerized surface is diminished toward tension while it increases under compression. More generally it can be stated that under tension, which is the case for growth on YSZ, the stability region of the stoichiometric surface is widened.

Finally, we note that for the hydroxylated surface this strong strain dependence is not observed. As a consequence, hydroxylation of films is even more likely in competition with peroxide formation under tension.

These findings have also implications in the context of gas-sensor applications. It can be assumed that the strain-dependent phase transitions can also lead to either a nanoparticle-size-dependent or a film-thickness-dependent gas response. It is also assumed that the findings can partly be transfered to (211) surfaces as well as to (111) [the edges of (111) have (001) character].

VII. DOPING EFFECT

A. Phase stability

Since in most technological applications Sn dopants are added to In_2O_3, understanding the role of n-doping in the context of surface structure and stability is of major interest.

When dopants are introduced into the material, two distinct effects have to be considered separately.

First, due to the presence of dopants the Fermi energy of the material is changed. This effect is especially pronounced in ITO where variations of the Fermi energy of $\Delta E_F > 1\,\text{eV}$ are possible. For this effect it is, however, important to recognize that the Fermi energy has no or only a minor influence on the energetics of charge-balanced surface reconstructions i.e. the surfaces which are usually stable. This is because the electronic states created at surfaces of more ionic compounds are to a large degree resonant with the host states of the material and cannot be filled or depleted for Fermi energies away from the band edges. As a result, the phase transitions between the stable surfaces presented in Sec. IV B are not expected to change because they obey electron counting rules and cannot accomodate extra charge at the surface (the metallic surface is an exception). Only the stability of charge unbalanced surfaces, which introduce additional states in the bandgap region, can be affected significantly.

A second effect is encountered when dopants are located at surface sites and directly interact with the surface species or change their electronic configuration and energy. It is possible, for example, that the oxidation state of a donor changes from the bulk to the surface. Such effects have been observed in the case of SnO_2, where the Sb dopants exhibit a lone-pair effect when located at the surface.[69]

To disentangle these two effects, we conducted a series of slab calculations with Sn donors at two different concentrations and with two different locations in the vicinity of (001-*M*) surfaces. For these studies we included the ground-state terminations, which we found for the pure material (metallic, stoichiometric, partial peroxide, and full peroxide terminations in Fig. 3). As stated, only a minor influence of the Fermi energy is expected for these surfaces and therefore we additionally included another three charge-unbalanced surface terminations in order to illustrate the effect of *n*-type doping.

One of these surfaces exhibits oxygen deficiency (4/12 oxygen per surface unit cell) whereas another has a surplus of oxygen (8/12 oxygen per surface unit cell). The third candidate is the peroxide surface of Sec. IV B with two dimers split into oxide ions (4 dimers and 4 oxygen per surface unit cell).

At this point, we focus on the (001) surface since its only for this orientation that stoichiometry variations appear to be relevant. We believe that the principal findings can be transferred to the (211) surface as it has some similarities with (001) surfaces (see Sec. II)

The calculated surface tensions with Sn are shown in the four panels of Fig. 8 (thick lines). The respective slab geometries are schematically indicated in the insets. In addition, all panels contain the reference phase diagram of *pure* In_2O_3 (thin black lines). All diagrams are energetically aligned to the corresponding stoichiometric (horizontal line segment) surfaces. This allows us to study variations of the phase boundaries due to the presence of dopants. The surface tension is now given as a relative value per surface unit cell. Note that the lines corresponding to the charge-unbalanced surfaces (not stable without dopants) are highlighted in red and significantly influenced by the dopants. The particular changes of individual surfaces are also indicated in the figures by arrows.

The two panels at the top of Fig. 8 show the result for tin dopants placed into the first (left) and the second (right) subsurface layers at a surface concentration of $c_A \sim 2\,\text{nm}^{-2}$. With the Sn atoms in the second layer the compositional domains for the phases (blue thick lines) hardly change, whereas the phase boundaries do shift when the Sn is located within the first surface layer. Evidently, tin atoms destabilize the dimerized surfaces and reduce their stability width compared with pure In_2O_3. This is denoted as a direct effect in the figure.

The behavior can be rationalized in terms of different electronegativities and sizes between Sn and In. Peroxides are generally stabilized by elements with low electronegativity as in, e.g., Na_2O_2 or BaO_2. Neither indium peroxide nor tin peroxide exists as a solid phase. The stability of tin peroxide, however, if it existed, would be lower on the basis of its higher electronegativity in comparison with In. Further, due to the size difference of the cations the dimers slightly distort, making the peroxide coverage even less commensurate than in the pure In case (see discussion in Sec. 7). In this context, it is also interesting to note that SnO_2 surfaces have already been studied in considerable detail and no peroxide-based surface termination could be identified by experiment and theory, which provides support for the above mentioned arguments.[46] Furthermore, peroxide-type point defects are less stable in SnO_2 when compared with those In_2O_3.[70]

Besides this *direct* effect, large changes in both phase diagrams can be identified for the charge-unbalanced terminations (red thick lines). The changes also coincide quantitatively for Sn in the first and second layers indicating the effect of only the Fermi energy. The changes are more pronounced for the oxygen-rich phases.

Going to higher doping concentrations (bottom part of Fig. 8) all effects mentioned before are enhanced in and can lead to new thermodynamically stable surface reconstructions (red lines appear below blue lines). The fact that these new surface phases appear more dominantly with tin in the first layer indicates also a segregation tendency of tin to the surface as described in more detail in Sec. VII B.

The donor-dopant-stabilized surfaces are generally characterized by a larger content of negative charge at the surface. This is plausible since the donor provides the electrons for the formation of the anions from neutral species and additionally exerts an electrostatic attraction. This can be achieved in different ways.

Starting from the full peroxide-covered surface this is possible by the splitting of the dimers into oxide anions:

$$O^{2-}_{2,\text{surf}} + 2e^- \rightleftharpoons 2O^{2-}_{\text{surf}}. \tag{8}$$

Starting with a stoichiometric surface this is achieved by an additional attachment of oxide anions,

$$O_2^{\text{gas}} + 4e^- \rightleftharpoons 2O^{2-}_{\text{surf}}, \tag{9}$$

and only to a lesser extent by the attachment of additional peroxide anions,

$$O_2^{\text{gas}} + 2e^- \rightleftharpoons 2O^{2-}_{2,\text{surf}}, \tag{10}$$

because they are destabilized by the tin dopants in the first surface layer. Additional peroxide attachment to fully

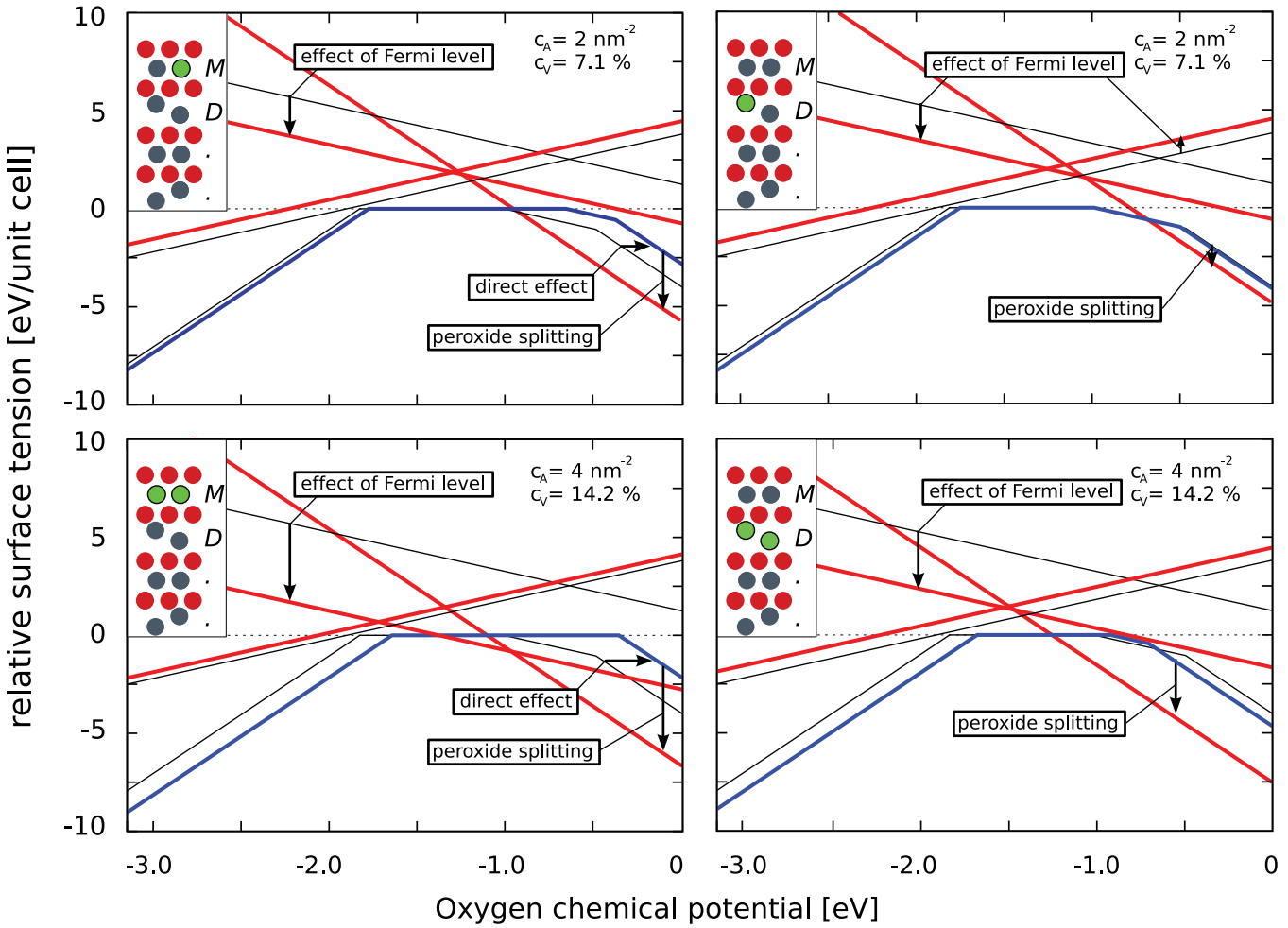

FIG. 8. (Color online) Phase diagrams of the (001-M) surface with a tin surface concentration of $c_A \sim 2\,\mathrm{nm}^{-2}$ (top) and $c_A \sim 4\,\mathrm{nm}^{-2}$ (bottom) with the dopants located in the first (left) and second (right) cation planes. The setup is schematically illustrated for each case. The green atoms represent the dopants in the insets. Thin black lines correspond to surfaces of pure In_2O_3 whereas thick lines show the surfaces with Sn dopants. The charge unbalanced surfaces (unstable for pure In_2O_3) are highlighted in red. All surface tensions are normalized to their respective stoichiometric surfaces (horizontal lines).

peroxide-covered surfaces is not favorable because of the low electrostatic interaction between the peroxide molecules and the surface cations in this case. The attachment of additional peroxide anions can occur only if the molecules are not flat but oriented perpendicular to the surface for geometrical reasons.

An interesting analogy is that the equilibria described by these reactions equivalently occur in the bulk of the material as well. Equation (9) corresponds to the defect model proposed by Frank and Köstlin[8] and the peroxide defects have been described in recent density functional theory (DFT) defect calculations.[71]

At the surface this mechanism is also equivalent to the so-called ionosorption model on semiconductors.[72,73] Within this model the surface terminations of ITO are obtained by ionosorbing additional oxide anions to the stoichiometric surface of pure In_2O_3.

We remark that the actual ionosorbed species are O^{2-} and not O^-. This result was verified by explicitly checking the oxidation state and magnetic moment of oxygen on such surfaces.

B. Segregation

In the previous section the absolute values of surface tensions were abandoned in order to study the effect of dopants on the phase transitions. However, the absolute surface tensions also vary with the concentration of dopants located within the surface. In the case of ITO, where large contents of dopants are used, their segregation can lead to a significantly reduced surface tension, which is also observed in experiments.[21]

The segregation energy is defined as the energy difference between a dopant in the surface and in the bulk,

$$E_{\mathrm{seg}} = E_{\mathrm{Sn-surf}} - E_{\mathrm{Sn-bulk}}, \tag{11}$$

and can be understood as the gain or loss of surface tension per dopant atom. Table IV summarizes the calculated values for various surface orientations and also different surface compositions. For (111) and (011) surfaces the segregation energy is predominantly positive. In the case of (111), the sixfold In sites on the surface, especially those at the origin

TABLE IV. Segregation energies of Sn on (111), (011), and (001) surfaces (in eV/Sn). For (111) and (011) the index corresponds to Sn located on the respective site in Fig. 2. In the case of (001) the index corresponds to the phases in the following ways: (1) metallic, (2) 1/3 oxygen, (3) partial peroxide (1/3 O, 1/6 dimers), (4) partial peroxide (1/6 O, 1/3 dimers), (5) stoichiometric, (6) full peroxide, (7) 2/3 oxygen termination. The segregation energies are given for two different tin concentrations in the case of the (001) surface.

				(001 − M)	
Site	(111)	(011)	Surface	2 nm^{-2}	4 nm^{-2}
In_I	−0.54	0.65(7)	1	−0.36	−0.55
In_{II}	0.15	0.75(4)	2	−0.42	−0.59
In_{III}	0.00	−0.15(9)	3	−0.04	−0.20
In_{IV}	0.44	–	4	0.18	−0.09
In_V	−0.19	–	5	−0.39	−0.51
In_{VI}	0.46	–	6	0.24	0.10
In_{VII}	0.19	–	7	−0.47	−0.79

in Fig. 2, have negative segregation energies whereas for all fivefold In the values are significantly positive.

As with water dissociation, the segregation of Sn at (111) surfaces is spatially selective and offers an interesting way of functionalizing this surface. A similar behavior is found for (011) surfaces with the segregation energies being even more positive. A slightly negative energy is found for Sn at the fivefold coordinated In site. Generally, the segregation energy on (111) and (011) surfaces is more negative when bound to a larger number of undercoordinated oxygen. Note that a lone-pair effect (Sn^{2+}) is not observed for Sn on these surfaces.

In contrast to these latter surfaces, a large energy gain is associated with tin beneath the (001) surfaces. An energy gain of up to 0.8 eV/Sn is observed especially for oxygen-rich surfaces. Note that the segregation energies for (001) surfaces are taken as differences between Sn in the first and second layers. The resulting segregation energy is therefore likely to be underestimated. The two positive values in Table IV for (001) surfaces are always in conjunction with full or partial peroxide surfaces and consistent with the peroxide destabilizing property of tin discussed in Sec. VII A.

Note that the segregation energies for (001) surfaces are given for two different Sn surface concentrations. This is necessary because the oxidation state of the topmost oxygen anions critically depends on the availability of electrons donated by Sn. For this reason the segregation energies increase with Sn content at some surfaces. In reality the necessary electrons could be provided by the bulk of the material which in a slab calculation is severely limited in size and therefore not possible unless the concentration of Sn is high enough. Accordingly, oxygen-rich surfaces can capture electrons from the (n-type) bulk of the material and therefore exhibit an electron depletion at the surface.

The attraction of Sn dopants to oxygen-rich (nonperoxide) surfaces can simply be understood on the basis of electrostatic arguments. Remarkably, a segregation tendency is also observed for oxygen-poor surfaces. In this case, the driving force cannot be an ionic interaction but is the lone-pair localization and formation of Sn^{2+} instead of Sn^{4+}. This observation is of experimental interest, because the lone-pair effect is exclusively observed on oxygen-deficient (001) surfaces, while it is not observed for any other orientation (except oxygen-deficient (211)). This finding offers a device for the identification of reduced ITO (001) surfaces, if it is possible to assign deep gap states on ITO surfaces to originate from Sn centers.

Finally, the results of the current and previous sections also offer a possible explanation why the (001) orientation of films is more predominant in the case of ITO, but very difficult to obtain in the case of pure In_2O_3. Taking a tin surface composition of 50%, the surface tension of the (001) surfaces can go below that of the (111) surface for oxygen-rich but also for oxygen-poor conditions. To see this, one can add the segregation energy per Sn (of the stoichiometric surface) to the phase diagrams of Fig. 8 (the phase diagrams were previously aligned to the corresponding stoichiometric surfaces).

A surface concentration of 50% seems relatively large; however, the electrostatic interaction is a long-range effect so that energy gain is also associated with Sn in deeper subsurface regions. The exact evaluation of the surface tension is difficult unless the distribution of tin and the corresponding band bending are known in the near-surface region. Evidently this distribution depends on the deposition and can be altered with the oxygen partial pressure,[21] which has also been demonstrated in experiments.

VIII. ELECTRONIC STRUCTURE

A. Electronic structure and band bending

1. (111) and (011) surfaces

In Sec. IV B it was shown that the surfaces of In_2O_3 can by reduced and oxidized. This is a rather different behavior in comparison with that of SnO_2, which can only be reduced. In the case of SnO_2, the reduction is possible by the formation of Sn^{2+} instead of Sn^{4+}. Also indium has a lone-pair effect which is, however, much weaker. Within the group III elements it is only Tl which has a dominant +1 oxidation state instead of +3 even though In(I) compounds do exist.[74] The predominant oxidation state is important for both, in the context of surface gap states, but also the STM contrast which can be expected for a particular surface[75] and also presented in the next section.

In the case of the predominantly stoichiometric surfaces [(111) and (011)], we have confirmed by means of Bader charge analysis the expected formal oxidation states of +3 and −2 for In and O, respectively, also for the surface species. These surfaces can be reduced at a relatively low oxygen chemical potential only and remain stoichiometric to a large extent.

Generally, due to the undercoordination of the cations on these stoichiometric surfaces the In-5s states are lowered and attain a higher density of states (DOS) at the bottom of the conduction band (CB). In Fig. 9 the site and l-decomposed electronic DOS of indium cations is presented for sixfold and fivefold coordinated cations on the (111) surface as well as sixfold, fivefold and fourfold coordinated cations on the (011) surfaces (in this case sixfold coordination corresponds to a bulk atom). Consistently, the undercoordinated In atoms show an increasing s-contribution to the bottom of the CB. Since

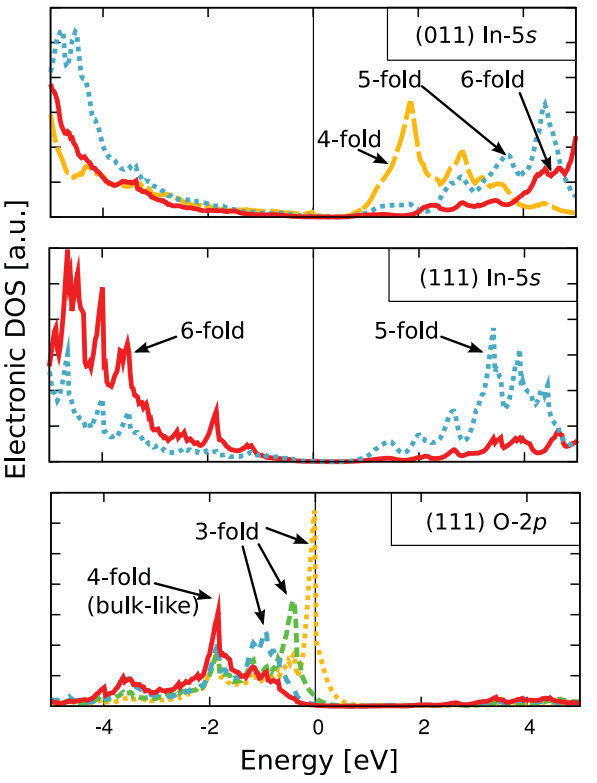

FIG. 9. (Color online) The partial electronic DOS of In-5*s* states for (011) and (111) surfaces as well as the O-2*p* states of oxygen atoms on the (111) surface. Note that the In-4*d* semicore states are not included in the valence.

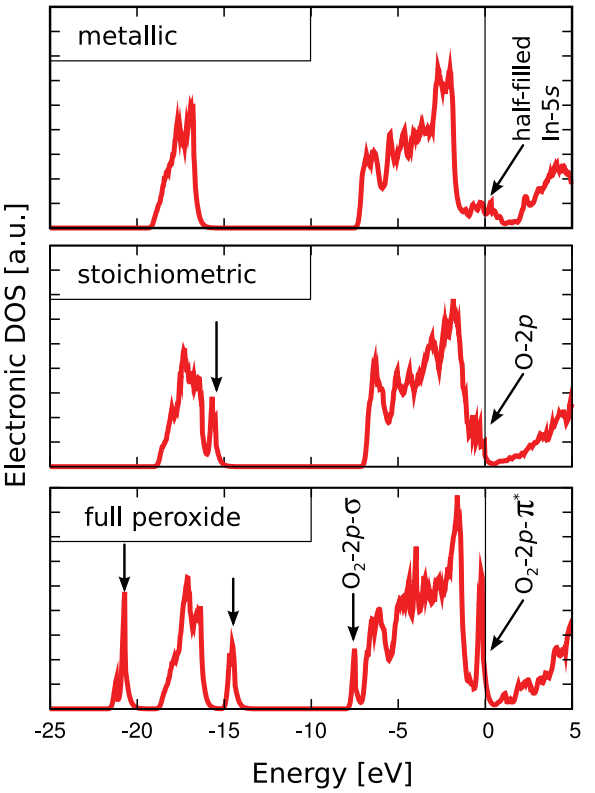

FIG. 10. (Color online) Total electronic DOS for the metallic, stoichiometric, and full peroxide terminations on In_2O_3 (001-*M*). The surface states are indicated with arrows. Note that the In-4*d* semicore states are not shown.

in the case of In_2O_3 the Fermi energy is usually found rather close to the conduction band minimum (CBM), these surface resonances at the CBM have an important implication because they can capture electrons from the CB in the bulk and act as acceptors, as proposed by Klein.[20] As a consequence (111) and (011) surfaces of In_2O_3 should exhibit an electron depletion at high Fermi energy. The effect, however, is weak because it is caused by an increased DOS of CB states at the surface. At more reducing conditions this depletion is likely to be dominated by a second effect.

In Sec. IV B we have shown that oxygen vacancies are more easily formed on (111) and (011) surfaces than in the bulk[76,77] (formation energies are always positive in the bulk). This is indicated by the existence of reduced surfaces at low oxygen chemical potentials in the phase diagrams (Fig. 3). It was pointed out that the nature of these reduced (111) and (011) surfaces can simply be described by an accumulation of oxygen vacancies. Oxygen vacancies are, however, also created at higher oxygen chemical potentials in large numbers. In a full thermodynamic equilibrium the oxygen vacancy concentration is always significantly higher in these (111) and (011) surfaces when compared with the bulk.

When surface vacancies are created more fivefold and fourfold In is produced as well. In addition, a positive surplus surface charge develops since oxygen vacancies are donors. The increased donor concentration toward the surface layer should effectively lead to an electron accumulation in this material which has already been measured.[25] Such an accumulation layer is sensitive not only to the bulk Fermi level position but also to the degree of equilibration of the sample as well as the environmental conditions under which it is measured because it is a consequence of surface reduction.

The heavily reduced (111) and (011) (Fig. 3) surfaces consist of vacancy clusters which produce increasingly deeper and overlapping states at the surface. It is intersting that there is no evidence of a lone-pair localization but an increased number of metallic bonds.

Also for oxygen surface resonances are observed. They can be found close to the valence band minimum (VBM), at (111) and (011) surfaces. Figure 9 shows the oxygen 2*p* states as they move toward the bandgap from the valence band (VB) when oxygen becomes increasingly undercoordinated. The different lines in the figure correspond to different oxygen species at the surface and the highest lying O-2*p* states correspond to the oxygen ions labeled O-I in Fig. 2. Because the Fermi energy is usually high in In_2O_3, these states always remain occupied and cannot cause band-bending effects.

2. The (001) surface

In the case of (001) surfaces, there are three major regimes when going from reduced to oxidized surfaces. Figure 10 shows the total DOS for the cation-terminated, stoichiometric, and fully peroxide-covered surfaces. In all cases gap states appear, however, originating from different species.

For the cation-terminated surfaces In-5*s*-derived and half-filled metallic bands are found within the bandgap and the

effective oxidation state of the cations is 1.5 according to Bader analysis. It is difficult to estimate the position of these states with respect to the band edges as they extend throughout the bandgap within the LDA. Since these states are only partially filled and the Fermi energy is usually found at or even above the CBM, these gap states should have an acceptor character causing an upward band bending for this surface.

In the case of ITO, Sn behaves differently compared with surface In. The Sn derived surface states on this metallic surface is related to the Sn lone pair (Sn^{2+}) and located below the In-related surface states from which it can captures electrons. This explains the segregation tendency of Sn at metallic surfaces (Sec. VII B). Thus Sn^{2+} leads to a saturation of the surface states, dampening the electron depletion effect which would otherwise occur at cation terminated (001) surfaces.

On the stoichiometric (001) surface the (filled) gap states originate from the O-2p of the topmost oxygen atoms, similar to (111) and (011) surfaces. In this case, however, they are located higher above VBM and clearly split off from the host states. This is because of the lower coordination number of oxygen (twofold) in comparison with (111) and (011) surfaces (threefold and fourfold). The dispersion of the states is low, as expected for oxygen. The width of the gap feature arises because oxygen are located at different elevations normal to the surface, resulting in a variation of the electrostatic potential.

In the case of the peroxide surface, the (filled) gap states originate from the antibonding $p - \pi^*$ orbitals of the dimers. The bonding $p - \sigma$ orbitals can be found as additional features at the bottom of the VB. Finally, due to the close proximity of the oxygen in the dimers, their corresponding O-2s states split significantly ($\sim$5 eV). A more detailed discussion on the electronic structure of peroxide defects in In_2O_3 can be found in Ref. 71.

We stress that in In_2O_3 or ITO the Fermi energy is usually found rather high in the bandgap. In particular it is high in comparison with the oxygen-related surface states of stoichiometric and peroxide surfaces which are shown in Fig. 10. The introduction of empty states with this energetic position (oxygen atoms or molecules) would lead to their immediate occupation so that they act as acceptors. The energy gain associated with this addition of oxygen and the capture of electrons from the CB of the material has been demonstrated already in Sec. VII B and resulted in additional surface structures and surface segregation of dopants. Therefore the oxygen-rich (001) surfaces of In_2O_3/ITO should also exhibit an electron depletion at the surface, in contrast to the findings of King *et al.*[24]

The (001) surfaces exhibit a chemically rather complex behavior so that we have to consider also the possibility of electron accumulation under certain conditions. In the case of stoichiometric (001) surfaces with low Fermi energy (no ionosorption of oxygen possible) the predominant defect mechanism at the surface could be oxygen vacancy creation similar that of to the (111) and (011) surfaces. In this case an electron accumulation could be possible. We believe, however, that for the majority of cases it is more likely to encounter an electron depletion, which is in marked contrast to (111) and (011) surfaces which should predominantly exhibit electron accumulation.

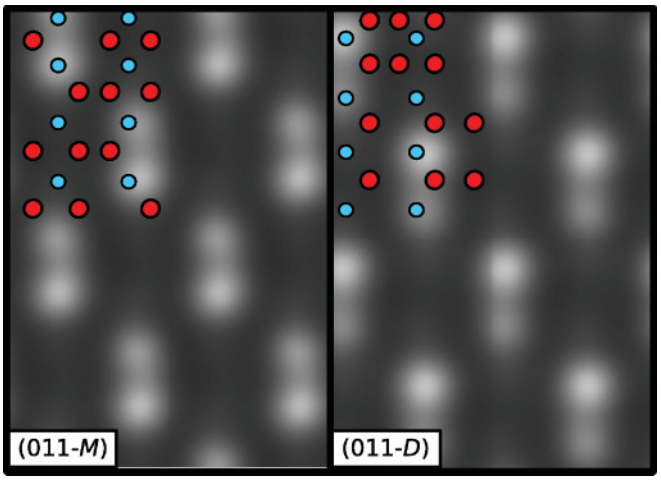

FIG. 11. (Color online) STM image simulation of stoichiometric (011−M) and (011−D) surfaces at +1.8 V. The atomic arrangement of the surface layer is shown. Bright features originate only from fourfold coordinated cations.

B. STM contrast

The atomic arrangement on In_2O_3 surfaces has been studied by Morales and co-workers for the (111)[37] and (001) surfaces[34] using STM techniques. In the first case, they found a simple and stoichiometric bulk truncation in good agreement with their STM image simulation and our calculated phase diagram (Fig. 3).

On the (001) surface they have found a considerably larger number of surface features. The resulting contrast of the empty-states STM was interpreted on the basis of previous theoretical investigations.[27,42] Specifically, what is termed as the (001-M) full peroxide termination in Sec. IV B of the present study was first presented by Zhou *et al.*[42] and taken as the basic pattern for the interpretation of the STM images. Here we discuss the essential STM features that can be expected for the various surfaces and specifically address the In_2O_3 (001) surface, for which experimental data are available.

1. Stoichiometric (011) surfaces

Generally, it is assumed that in empty-states STM, bright contrast mainly originates from the cations, since the CB is derived from extended In-5s states. However, the actual atomic coordination of the surface cations is variable and has an additional effect on the relative brightness of the surface species. The In-5s states tend to lower in energy when the coordination number of the cations is decreased. This is well illustrated in a simulated STM image of the stoichiometric (011) surface (Fig. 11) where fivefold and fourfold coordinated In can be found at essentially equal heights in normal directions to the surface.

For both (011-M) and (011-D) the bright contrast originates only from fourfold In whereas fivefold In is much darker. As expected, oxygen is invisible although it is located at similar altitude. Note that the TH-STM image is obtained using a bias voltage of $V_{bias} = +1.8$ V, and there is no great influence of the parameter on these essential features.

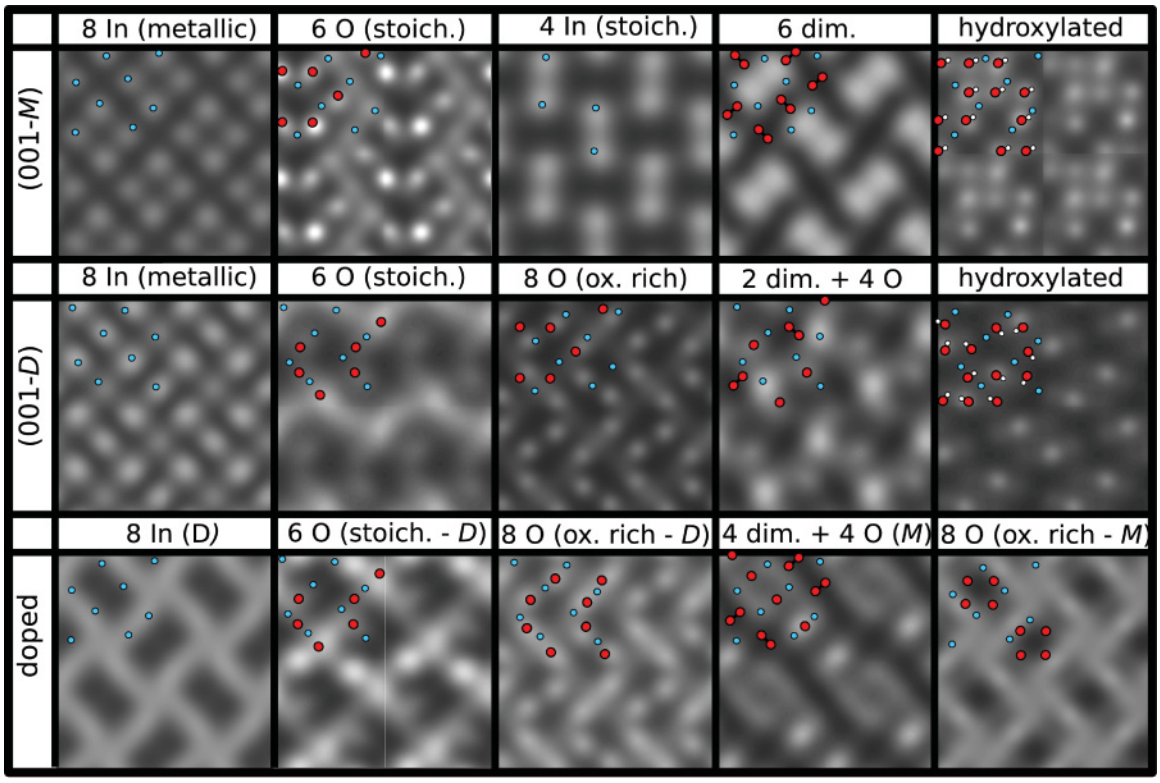

FIG. 12. (Color online) STM image simulation of various In_2O_3 (001) surfaces at a bias of +1.8 V. The first, second, and third rows contain (001-M), (001-D) and doped (001-M/D) surfaces. The labels denote the content of surface species per cubic surface unit cell. The bulk truncations correspond to either 8 In or 12 O.

2. The (001) surfaces

In the case of the (001) orientation, additional difficulties in the interpretation of STM images arise because of the large variety of different surface phases (see Fig. 2), but also due to the alternating stacking sequence (see Fig. 1) with cations and anions at different heights. As a result there is a competition between surface topography and local electronic structure. STM simulations for a collection of different (001) surfaces are presented in Fig. 12 showing the diversity of observable patterns. The bias voltage was always kept at +1.8 V. The positions of several atoms on the surface are marked in the images. Figure 12 covers both (001-M) (first row) and (001-D) (second row). For the last set of pictures (third row) in Fig. 12 Sn was present in the slab to illustrate the effect of n-doping.

It is well known that Sn dopants hardly change the electronic structure of In_2O_3, despite their large concentration. The dopants, however, drastically affect the Fermi energy position of the material even to energies significantly beyond the CBM. This occupation of CB states (Burstein–Moss shift) can lead to *unavailable* empty states for STM sampling and a potentially changed contrast. Generally, n-doping has an effect similar to an increased bias voltage since a larger fraction of higher lying states are sampled in both cases. This approximate analogy is also in line with the way the STM images change upon n-doping. Apart from the Fermi energy, Sn dopants have only a minor influence on the STM contrast and are not expected to be distinguishable from In.

3. Metallic (001) surfaces

On the fully cation-terminated surface, bright contrast simply indicates the location of the In cations. Already in this case, additional features appear between the In cations, leading to slightly different appearances for (001-M) and (001-D), respectively. It is also noteworthy that these additional features are enhanced at higher voltages. Although the interpretation seems to be simple, the observed contrast is rather surprising because this surface has partially occupied In-5s states deep in the bandgap. Since the Fermi energy is generally high in In_2O_3/ITO, these surface states may be fully occupied and lead to a very different contrast, as depicted in the third row of Fig. 12. No single atoms can be identified but bright bands run along the ⟨110⟩ direction. This is the effect of the more directional In-5p contribution to the empty states.

4. Stoichiometric (001) surfaces

When oxygen is brought onto the terminal cation layer it is tempting to assume that the height difference of >1.2 Å between oxygen and indium planes is sufficient to produce a bright contrast by only the oxygen species located in the topmost layer. As a general result such an assumption cannot be sustained on the basis of the STM image simulations.

In the case of the stoichiometric terminations (six oxygen per surface unit cell) some oxygen can be associated with bright features, but not exclusively. A large amount of the bright contrast originates from the underlying cation layer. The resulting images are generally difficult to interpret and

change massively with the actual oxygen distribution on the terminal layer. This is important since for thermodynamic reasons a disorder is expected for theses surfaces. The calculated images show only the lowest-energy structures which we could identify.

Common to many of these structures are, however, similar bright crosslike features as found for the n-doped metallic terminations. These features are often only rudimentarily present and appear as zigzag bands running along $\langle 001 \rangle$. Again, these features tend to be enhanced at higher voltages but also by n-doping.

In summary, the competition of electronic structure versus the topography in the case of stoichiometric oxygen terminated surfaces is determined by the detailed arrangement of the surface oxygen as well as by the sampling parameters making an unambiguous identification difficult. For comparison, the lowest-energy half-indium termination is also shown in the first row of Fig. 12. The contrast produced by this surface suggests that it can very well be distinguished from the stoichiometric half-oxygen reconstructions.

5. Peroxide (001) surfaces

For undoped In_2O_3 and on the oxygen-rich side, the full or partial peroxide surface terminations are predicted to be thermodynamically favorable. In comparison with oxide anions on the stoichiometric surfaces, the peroxide anions undergo a more pronounced inward relaxation, bringing them closer to the underlying cation plane. As a result, the peroxide terminations exhibit no bright contrast at the location of the peroxo-ions anymore, whereas it is partially the case for the oxide anions on stoichiometric surfaces. Additionally, the splitting of the σ states in the covalent bond of the dimers results in oxygen states that are inaccessibly high for tunneling. While the peroxide dimers constitute the topmost layer, the bright contrast originates from the indium cations located in the second layer. This behavior does not change with a varying bias or sampling height. In fact, the dimers are located within the darkest areas of the image. The STM images of surfaces containing both peroxo-anions and oxide anions, (2 dim +4 O and 4 dim +4 O) illustrate directly the relative brightness of the two anionic species. For example, the surface containing four dimers and four oxide anions is created by splitting two dimers from the full peroxide termination. Additional bright features appear at the locations where the dimers were split.

In the case of n-type doping, surfaces with less peroxide species but more oxide anions are thermodynamically more stable (see Sec. VII). Also, for these non-charge-balanced oxygen-rich surfaces, STM images are shown. Such surfaces are stabilized only by n-doping (8 O-D/M, 4 dim +4 O). The images are characterized again by crosslike and zigzag-like patterns and the contrast depends on the actual arrangement of the oxygen species. From thermodynamic considerations, these structures should be among the most stable surfaces for ITO under oxygen-rich conditions. Also in this case, however, it should be noted that the images are not unique due to the disordered nature of these terminations.

6. Hydroxylated (001) surfaces

In the case of the hydroxylated surfaces for both (001-M) and (001-D), the interpretation is straightforward because the topmost hydrogen cations are bright. Since the hydrogen is tightly attached to the oxygen of the underlying oxygen layer, the hydrogen *brightens up* the oxygen ions which are located in their bulklike arrangement. Nevertheless, (001-M) and (001-D) surfaces appear distinct which is due to the structure of the underlying cation layer. While on (001-M) all hydroxyl groups are at similar elevation, there are four protruding hydroxyls on (001-D) surfaces. This difference results in 12 and 4 bright spots on (001-M) and (001-D), respectively.

7. Comparison with experiment

According to the STM image simulation, the fully hydroxylated (001), fully dimerized, and half-indium termination and to a lesser extent the full cation termination promise to have the highest degree of uniqueness for STM identification. These surfaces are not among those which were probably observed by Morales and Diebold.[34]

Their samples were exposed to oxygen-rich conditions prior to investigation and were highly doped. Additionally, the contamination with water can be excluded. With a relatively high confidence the majority of observed features cannot be assigned to peroxide-type terminations as it was believed before.

From thermodynamic reasoning and with the aid of STM image simulations we are in the position to propose an alternative interpretation. In short, we suggest surfaces terminated mainly with oxide anion species and oxygen overstoichiometry as described in Sec. VII. Under heavy n-doping these surfaces are thermodynamically most plausible. These surfaces also exhibit the largest energy gain by segregation of tin ions to the topmost cation layer. Heavily hydroxylated surfaces can be excluded on the basis of the preparation conditions but also of the TH images. In addition, for heavily hydroxylated surfaces we have checked by calculation that there is no segregation tendency for Sn. In turn, the adsorption of hydrogen species on doped samples is less likely when compared with that of undoped In_2O_3 surfaces.

Besides the thermodynamics, the proposed surfaces also produce an STM contrast which is in qualitative agreement with many of the experimentally observed features. Especially, the terminations labeled 8O-M and 8O-D closely resemble the observed structures with bright crosses and irregular zigzag bands. The surfaces found experimentally also involved a considerable degree of disorder which is expected for only this partially oxygen (oxide anions) terminated models. The occasional appearance of darker spots in the experiments could indicate the locations of remaining peroxide anions on the surface. Finally, we remark that the observed symmetry of the LEED pattern is also consistent with this interpretation, assuming a high degree of disorder.

IX. SUMMARY

We have investigated the thermodynamic stability of various surfaces and have found that the surface stability of stoichiometric In_2O_3 surfaces increases as $\gamma(111) < \gamma(011) < \gamma(211) < \gamma(001)$, which is consistent with observed shapes of nanoparticles[78] but not observed in the texturing of ITO films.

The most stable surfaces, [(111) and (011)] do not exhibit significant stoichiometric variations whereas surfaces with

polarity can be significantly off-stoichiometric. We observe the largest stoichiometry variations for the (001) surfaces, which partially resemble the chemistry of the (211) surfaces and step edges of (111) surfaces. In_2O_3 can sustain oxygen-rich surfaces which owe their stability to peroxide formation. Under oxygen-poor conditions the surfaces exhibit metallic states, often involving a strong overlap of In-5*s* states and in the absence of a clear lone-pair formation at the surface. While the most stable surfaces (111) and (011) are characterized by their chemical inertness, the (001) surfaces exhibit various surface phase transitions, which are sensitive to experimental boundary conditions.

Besides the chemical environment, the phase boundaries depend also on the in-plain strain. Because of the pronounced tensile surface stress due to the peroxide formation these surfaces exhibit large energy variations as a function of an external stress that can originate from interfaces in thin-film geometries. As a result the phase boundaries are shifted, disfavoring the peroxide surface terminations and widening the range of the stoichiometric disordered phase.

Under the influence of hydrogen a different compensation mode for the polarity of the (001) surface becomes active. The fully hydroxylated and oxygen-rich surface can attain a surface tension even lower when compared with all other intrinsic In_2O_3 terminations. The resulting surface is obtained by one monolayer of dissociative water adsorption on the stoichiometric surface even at elevated temperatures. While a high degree of hydroxylation is expected for (001) surfaces, water adsorption on (111) but also (011) is weak and locally restricted to a small fraction of the total surface area. Nevertheless, dissociative water absorption is still possible also on those surfaces.

An alternative to hydrogen and also other *n*-dopants influence the stability of the surfaces. In the case of a high tin doping new surface reconstructions appear as thermodynamic ground states and are influenced by two effects: the direct effect of the dopants which are in contact with the surface species on the one side and the effect of the Fermi energy only, for which the exact location of the dopant is not relevant, on the other side.

The direct effect tends to destabilize the peroxide anions whereas the higher Fermi energy generally stabilizes additional negatively charged species. Two new surface phases which should be observable only under *n*-doping have been presented in this context, and more are believed to exist due to the continuous transition with increasing Fermi energy and the disordered nature of these reconstructions.

In light of the thermodynamic assessment of In_2O_3 and ITO surfaces, a new interpretation of available experimental STM data has been suggested. By explicit STM image simulation it was found that on (001) surfaces the bright contrast is provided mainly by indium cations, hydrogen, and, to only a lesser extent, by oxide anions but not by peroxide anions. These findings lead to the reinterpretation of the existing experimental STM images. Instead of the peroxide-type reconstructions it appears more compelling to assume an off-stoichiometric (oxygen-rich) and disordered oxide ion termination, a surface which is not particularly stable in the case of pure In_2O_3 and stabilized only by *n*-doping.

As the most general and practical result the appearance of preferential (001) texturing of ITO samples was explained despite the highest surface tension of (001) surfaces in the case of pure In_2O_3. The combination of a high Fermi energy and oxygen-rich conditions together with the electrostatic energy gain due to Sn segregation and the probable high growth rates on (001) surfaces leads to the predominant (001) texturing of ITO samples.

X. CONCLUSION

In summary, we have extensively studied most of the experimentally observed In_2O_3/ITO surfaces and discussed the effects of environment (oxygen partial pressure and temperature), substrate mismatch as well as hydrogen and doping. Our results provide a comprehensive basis for future studies of In_2O_3 surfaces. Again, we emphasize the role of the Fermi energy on the surface stability, a parameter which is often neglected in related studies. Especially when the variability of this parameter can be large as in In_2O_3, it can have a determining role on the observed surface features.

With this comprehensive study, the possibilities as catalyst, gas-sensing, and electronic contact material can proceed in a more systematic way based on a sound microscopic approach. Especially, with the use of epitaxial In_2O_3/ITO, the rather distinct properties of different In_2O_3 surfaces can be exploited in the future.

For example, (001) surfaces provide a probably too-large variability of surface composition in order to serve well as gas sensors with predictable gas responses in a wide range of conditions. On the other hand, this variability is favorable for In_2O_3 being a combustion catalysis because the (001) surfaces can contain a large content of weakly bound oxygen species. In the context of contact materials not only the orientation[45] but also the surface composition can provide some variability for the ionization potentials and work functions.[29]

Also, in the field of nanoparticle research, our thermodynamic assessment of the surfaces can be of help. For example, the predominant equilibrium nanoparticle shapes are octahedra due to the low (111) surface tension. To produce more round-shaped nanoparticles it is advisable to obtain them at very reducing conditions where the surface energetics converge to very similar values for all surfaces (Fig. 3). In contrast, for cubic nanoparticles it is advisable to use *n*-doped In_2O_3 and in conjunction with either oxygen plasma or ozone exposure. Alternatively, synthesis routes from the hydroxide could also be successful in producing cubic particles with hydroxylated (001) faces.

ACKNOWLEDGMENTS

We acknowledge the financial support through the Sonderforschungsbereich 595 “Fatigue of functional materials” of the Deutsche Forschungsgemeinschaft. Moreover, this work was made possible by grants for computing time at FZ Jülich and on HHLR machines in Darmstadt and Frankfurt. Fruitful discussions with Andreas Klein, André Wachau, and Manuel Diehm are acknowledged.

*agoston@mm.tu-darmstadt.de

[1] L. S. Hung and C. H. Chen, Mater. Sci. Eng. R **39**, 143 (2002).
[2] C. J. Brabec, N. S. Sariciftci, and J. C. Hummelen, Adv. Funct. Mater. **11**, 15 (2001).
[3] H. Kim, C. M. Gilmore, A. Piqué, J. S. Horwitz, H. Mattoussi, H. Murata, Z. H. Kafafi, and D. B. Chrisey, J. Appl. Phys. **86**, 6451 (1999).
[4] P. Peumans, A. Yakimov, and S. R. Forrest, J. Appl. Phys. **93**, 3693 (2003).
[5] H. L. Hartnagel, A. K. J. Dawar, and C. Jagadish, *Semiconducting Transparent Thin Films* (Institute of Physics Publishing, Bristol, 1995).
[6] D. S. Ginley and C. Bright, MRS Bull. **25**, 15 (2000).
[7] T. Kamiya and H. Hosono, Int. J. Appl. Ceram. Technol. **2**, 285 (2005).
[8] G. Frank and G. Köstlin, Appl. Phys. A **27**, 197 (1982).
[9] T. Takada, K. Suzuki, and M. Nakane, Sens. Actuators B **13**, 404 (1993).
[10] T. Takada, H. Tanjou, T. Saito, and K. Harada, Sens. Actuators B: **25**, 548 (1995).
[11] A. Gurlo, N. Brsan, M. Ivanovskaya, U. Weimar, and W. Gpel, Sens. Actuators B: **47**, 92 (1998).
[12] S.-R. Kim, H.-K. Hong, C. H. Kwon, D. H. Yun, K. Lee, and Y. K. Sung, Sens. Actuators B: **66**, 59 (2000).
[13] A. Galdikas, Z. Martunas, and A. Setkus, Sens. Actuators B **7**, 633 (1992).
[14] H. Yamaura, T. Jinkawa, J. Tamaki, K. Moriya, N. Miura, and N. Yamazoe, Sens. Actuators B: **36**, 325 (1996), Proceedings of the Sixth International Meeting on Chemical Sensors.
[15] Y. Sawada and Y. Taga, Thin Solid Films **116**, L55 (1984).
[16] C. K. Choi, C. H. Margraves, S. I. Jun, A. E. English, P. D. Rack, and K. D. Kihm, Sensors **8**, 3257 (2008).
[17] J. Li, H. Fu, L. Fu, and J. Hao, Environ. Sci. Technol. **40**, 6455 (2006).
[18] P. Cox, W. Flavell, and R. Egdell, J. Solid State Chem. **68**, 340 (1987).
[19] A. Klein, A. Körber, C. Wachau, F. Säuberlich, Y. Gassenbauer, S. P. Harvey, and T. O. Mason, Thin Solid Films **518**, 1197 (2009).
[20] A. Klein, Appl. Phys. Lett. **77**, 2009 (2000).
[21] Y. Gassenbauer, R. Schafranek, A. Klein, S. Zafeiratos, M. Hävecker, A. Knop-Gericke, and R. Schlögl, Phys. Rev. B **73**, 245312 (2006).
[22] L. F. J. Piper, A. DeMasi, S. W. Cho, K. E. Smith, F. Fuchs, F. Bechstedt, C. Körber, A. Klein, D. J. Payne, and R. G. Egdell, Appl. Phys. Lett. **94**, 022105 (2009).
[23] A. Bourlange, D. J. Payne, R. G. Egdell, J. S. Foord, P. P. Edwards, M. O. Jones, A. Schertel, P. J. Dobson, and J. L. Hutchison, Appl. Phys. Lett. **92**, 092117 (2008).
[24] P. D. C. King, T. D. Veal, D. J. Payne, A. Bourlange, R. G. Egdell, and C. F. McConville, Phys. Rev. Lett. **101**, 116808 (2008).
[25] P. D. C. King, T. D. Veal, F. Fuchs, Ch. Y. Wang, D. J. Payne, A. Bourlange, H. Zhang, G. R. Bell, V. Cimalla, O. Ambacher, R. G. Egdell, F. Bechstedt, C. F. McConville,, Phys. Rev. B **79**, 205211 (2009).
[26] S. P. Harvey, T. O. Mason, Y. Gassenbauer, R. Schafranek, and A. Klein, J. Phys. D **39**, 3959 (2006).
[27] V. Golovanov, M. A. Mäki-Jaskari, T. T. Rantala, G. Korotcenkov, V. Brinzari, A. Cornet, and J. Morante, Sens. Actuators B **106**, 563 (2005).
[28] S. P. Harvey, T. O. Mason, C. Körber, Y. Gassenbauer, and A. Klein, Appl. Phys. Lett. **92**, 252106 (2008).
[29] M. V. Hohman, P. Agoston, A. Wachau, T. Bayer, J. Brötz, K. Albe, and A. Klein, J. Phys. Condens. Matter (in press).
[30] H. Ohta, M. Orita, M. Hirano, and H. Hosono, J. Appl. Phys. **91**, 3547 (2002).
[31] M. Kamei, H. Enomoto, and I. Yasui, Thin Solid Films **392**, 265 (2001).
[32] Y. Shigesato, S. Takaki, and T. Haranoh, J. Appl. Phys. **71**, 3356 (1992).
[33] A. Bourlange, D. J. Payne, R. G. Palgrave, H. Zhang, J. S. Foord, R. G. Egdell, R. M. J. Jacobs, T. D. Veal, P. D. C. King, and C. F. McConville, J. Appl. Phys. **106**, 013703 (2009).
[34] E. H. Morales and U. Diebold, Appl. Phys. Lett. **95**, 253105 (2009).
[35] R. E. Larson, Ph.D. thesis, Technische Universität Darmstadt, 2007.
[36] V. Brinzari, G. Korotcenkov, M. Ivanov, V. Nehasil, V. Matolin, K. Masek, and M. Kamei, Surf. Sci. **601**, 5585 (2007).
[37] E. H. Morales, Y. He, M. Vinnichenko, B. Delley, and U. Diebold, New J. Phys. **10**, 125030 (2008).
[38] E. J. Tarsa, J. H. English, and J. S. Speck, Appl. Phys. Lett. **62**, 2332 (1993).
[39] M. Kamei, T. Yagami, S. Takaki, and Y. Shigesato, Appl. Phys. Lett. **64**, 2712 (1994).
[40] M. Kamei, Y. Shigesato, and S. Takaki, Thin Solid Films **259**, 38 (1995).
[41] O. Bierwagen and J. S. Speck, J. Appl. Phys. **107**, 113519 (2010).
[42] C. Zhou, S. Chen, J. Wu, R. K. Heier, and H. Cheng, J. Phys. Chem. C **112**, 14015 (2008).
[43] Z. R. Xiao, X. F. Fan, L. X. Guan, C. H. A. Huan, J. L. Kuo, and L. Wang, J. Phys. Condens. Matter **21**, 272202 (2009).
[44] D. Fuks, D. Shapiro, A. Kiv, V. Golovanov, and C. Liu, Int. J. Quantum Chem. **111**, 1902 (2010).
[45] A. Walsh and C. R. A. Catlow, J. Mater. Chem. **20**, 10438 (2010).
[46] M. Batzill and U. Diebold, Prog. Surf. Sci. **79**, 47 (2005).
[47] G. Kresse, O. Dulub, and U. Diebold, Phys. Rev. B **68**, 245409 (2003).
[48] M. Marezio, Acta Crystallogr. **20**, 723 (1966).
[49] P. Agoston and K. Albe, Phys. Rev. B **81**, 195205 (2010).
[50] P. W. Tasker, J. Phys. C **12**, 4977 (1979).
[51] J. Goniakowski, F. Finocchi, and C. Noguera, Rep. Prog. Phys. **71**, 016501 (2008).
[52] G. Kresse and J. Furthmüller, Phys. Rev. B **54**, 11169 (1996).
[53] G. Kresse and J. Furthmüller, Comput. Mater. Sci. **6**, 15 (1996).
[54] D. M. Ceperley and B. J. Alder, Phys. Rev. Lett. **45**, 566 (1980).
[55] P. E. Blöchl, Phys. Rev. B **50**, 17953 (1994).
[56] G. Kresse and D. Joubert, Phys. Rev. B **59**, 1758 (1999).
[57] R. F. W. Bader, *Atoms in Molecules—A Quantum Theory* (Oxford University Press, Oxford, 1990).
[58] J. Tersoff and D. R. Hamann, Phys. Rev. B **31**, 805 (1985).
[59] A. Hinchecliffe, *Chemical Modeling: Applications and Theory* (RSC Publishing, Cambridge, UK, 2006), Vol. 4.
[60] K. Reuter and M. Scheffler, Phys. Rev. B **65**, 035406 (2001).
[61] D. R. Lide, *Handbook of Chemistry and Physics* 85th edition (CRC Press, Boca Raton, FL, 2005).
[62] J. P. Perdew, K. Burke, and M. Ernzerhof, Phys. Rev. Lett. **77**, 3865 (1996); **78**, 1396(E) (1997).
[63] D. R. Stull and H. Prohet, *JANAF Thermochemical Tables*, 2nd ed. (U. S. National Bureau of Standards, Washington, DC, 1971).

[64]K. Sugiyama, H. Ishii, Y. Ouchi, and K. Seki, J. Appl. Phys. **87**, 295 (2000).
[65]F. Esch, S. Fabris, L. Zhou, T. Montini, C. Africh, P. Fornasiero, G. Comelli, and R. Rosei, Science **309**, 752 (2005).
[66]A. Gurlo, D. Dzivenko, P. Kroll, and R. Riedel, Phys. Status Solidi Rapid Res. Lett. **2**, 269 (2008).
[67]D. F. Mullica, G. W. Beall, W. O. Milligan, J. D. Korp, and I. Bernal, J. Inorg. Nucl. Chem. **41**, 277 (1979).
[68]R. Shuttleworth, Proc. Phys. Soc. A **63**, 444 (1950).
[69]R. Egdell, W. Flavell, and P. Tavener, J. Solid State Chem. **51**, 345 (1984).
[70]P. Agoston, C. Körber, M. J. Puska, R. M. Nieminen, A. Klein, and K. Albe, J. Appl. Phys. **108**, 053511 (2010).
[71]P. Agoston, P. Erhart, A. Klein, and K. Albe, J. Phys. Condens. Matter **21**, 455801 (2009).
[72]K. Hauffe, Angew. Chem. **68**, (1956).
[73]H. Geistlinger, Sens. Actuators B **17**, 47 (1993).
[74]A. F. Holleman, E. Wiberg, and N. Wiberg, *Lehrbuch der Anorganischen Chemie* (Walter de Gruyter & Co., Berlin, 1995).
[75]P. Agoston and K. Albe, Surf. Sci. **605**, 714 (2011).
[76]S. Lany and A. Zunger, Phys. Rev. Lett. **98**, 045501 (2007).
[77]P. Agoston, K. Albe, R. M. Nieminen, and M. J. Puska, Phys. Rev. Lett. **103**, 245501 (2009).
[78]Y. Hao, G. Meng, L. Ye, and C. Zhang, Cryst. Growth Des. **5**, 1617 (2005).